Fundamentals of Soft, Stretchable Heat Exchanger Design

by

Praveen Kotagama

A Dissertation Presented in Partial Fulfillment
of the Requirements for the Degree
Doctor of Philosophy

Approved May 2020 by the
Graduate Supervisory Committee:

Konrad Rykaczewski, Chair
Robert Wang
Patrick Phelan
Marcus Herrmann
Matthew Green

ARIZONA STATE UNIVERSITY

December 2020

ABSTRACT

Deformable heat exchangers could provide a multitude of previously untapped advantages ranging from adaptable performance via macroscale, dynamic shape change (akin to dilation/constriction seen in blood vessels) to enhanced heat transfer at thermal interfaces through microscale, surface deformations. So far, making deformable, 'soft heat exchangers' (SHXs) has been limited by the low thermal conductivity of materials with suitable mechanical properties. The recent introduction of liquid-metal embedded elastomers by Bartlett et al[1] has addressed this need. Specifically, by remaining soft and stretchable despite the addition of filler, these thermally conductive composites provide an ideal material for the new class of "soft thermal systems", which is introduced in this work. Understanding such thermal systems will be a key element in enabling technology that require high levels of stretchability, such as thermoregulatory garments, soft electronics, wearable electronics, and high-powered robotics. Shape change inherent to SHX operation has the potential to violate many conventional assumptions used in HX design and thus requires the development of new theoretical approaches to predict performance. To create a basis for understanding these devices, this work highlights two sequential studies. First, the effects of transitioning to a surface deformable, SHX under steady state static conditions in the setting of a liquid cooling device for thermoregulation, electronics and robotics applications was explored. In this study, a thermomechanical model was built and validated to predict the thermal performance and a system wide analysis to optimize such devices was carried out. Second, from a more fundamental perspective, the effects of SHXs undergoing transient shape deformation

during operation was explored. A phase shift phenomenon in cooling performance dependent on stretch rate, stretch extent and thermal diffusivity was discovered and explained. With the use of a time scale analysis, the extent of quasi-static assumption viability in modeling such systems was quantified and multiple shape modulation regime limits were defined. Finally, nuance considerations and future work of using liquid metal-silicone composites in SHXs were discussed.

DEDICATION

Dedicated to my family, girlfriend, friends, mentors and cat (Poperroni)

ACKNOWLEDGMENTS

I would like to thank my adviser, Dr Konrad Rykaczewski, for affording me this truly fascinating opportunity and for his patience in dealing with the numerous blunders I made under his mentorship. A special thanks to my lab mates, Kenneth Manning and Akshay Phadnis, without whom my PhD would have undoubtedly taken twice as long and I would be half the engineer I am today. I thank my committee members for their invaluable discussions in this work. Finally, I gratefully acknowledge funding from the National Science Foundation through award number CBET #1724452.

TABLE OF CONTENTS

Page

LIST OF FIGURES vii

CHAPTER

1. INTRODUCTION 1

1.1 Motivation 1

1.2 Summary and Outline 2

2. THERMAL PERFORMANCE OF A STATIC, STEADY STATE, SOFT HEAT EXCHANGER 5

2.1 Experimental Section 8

2.1.1 The Composite Tube Fabrication 8

2.1.2 Measurement of the Cooling Capability of the Composite Tubes 10

2.1.3 Mechanical Characterization of the Silicone Composites 12

2.1.4 Thermal Characterization of the Silicone Composites 13

2.1.5 Sample Imaging Procedures 14

2.2 Results and Discussion 15

2.2.1 Composite Models and Measured Properties 15

2.2.2 Thermomechanical Model of Tube's Thermal Resistance and its Validation 18

2.2.3 Strategies for Improving Cooling Capability of Tubes in Contact with Metallic Substrates 22

2.2.4 Model Based Strategies for Improving Cooling Capability of Tubes

CHAPTER Page

in Contact with Skin 28

2.2.5 Impact of Low Resistance Tubing on Overall Cooling System 30

2.3 Summary 33

3. SOFT HEAT EXCHANGERS UNDERGOING LARGE DEFORMATION DURING OPERATION 35

3.1 Experimental Methods 37

3.1.1 Soft Heat Exchanger Fabrication 37

3.1.2 Thermal Characterization 38

3.1.3 Testing Procedure 39

3.1.4 Experimental Considerations and Raw Data Analysis 41

3.2 Results and Discussion 45

3.2.1 Time-Scale Analysis of the Soft Heat Exchanger Operation 45

3.2.2 Thermofluidic Characterization of Soft Heat Exchanger Operation 46

3.2.3 The Characteristic Time Scale Ratio and Shape-Modulation Regimes 50

3.3 Summary 55

4. CONCLUSIONS AND FUTURE WORK 57

REFERENCES 63

APPENDIX 69

A. SUPPORTING INFORMATION FOR CHAPTER 2 69

B. SUPPORTING INFORMATION FOR CHAPTER 3 84

C. COPYRIGHT PERMISSIONS 92

LIST OF FIGURES

Figure Page

2.1 Illustrations of a) an Upper Body Liquid-Cooled Jacket Layout, b) a Corresponding Cross-Section of the Tube Interface With Skin (Fabric Is Assumed to Be Located on Outer Part of the Tube), c) Liquid-Cooled Jacket Used to Cool Motors Within a Robotic Leg, and d) a Corresponding Cross-Section of the Tube Interface With the Motor. T_{m,H_2O}, $T_{m,in}$, $T_{m,out}$ Stand for Mean, Mean Inlet, and Mean Outlet Water Temperatures, and R_{conv}, R_{tube}, R_{int}, R_{body} and R_{motor} Stand for Convective, Tube, Interface, Body, and Motor Thermal Resistances, Respectively. 6

2.2 Illustrations of a) the Casting Procedure and the Dimensions of the Mold, the Exploded View of b) the Experimental Setup and c) the Hotplate Configuration With Sensor Placements Indicated, d) Photograph and Schematic Cross-Sectional View of the Device, with Indicated Dimensions ($h = 4\ mm$, $z = 2\ mm$, $D_i = 2\ mm$ and $w = 5.5\ mm$). 9

2.3 a) Representative SEM Image of the Aluminum Particles; Plots of the Measured Composite b) Thermal Conductivity (k_c), c) Shear Modulus (G_c), d) and Young's Modulus (E_c) as a Function of Volumetric Filler Content ϕ Compared Against the Corresponding Theoretical Model. 16

2.4 Plots Comparing the Measured and Predicted Total Thermal Resistance for Meter of Tubing of the Liquid-Cooled Devices in Contact With the Hotplate at a) Low and b) High Contact Pressure. The Predictions of the Sub Models of Tube

(R'_{tube}), Interface (R'_{int}), and Interface With Liquid Metal Filler Are Also Included (R'_{LM-int}) as Indicated by the Diverging Purple Shaded Area. c) The Variation of R'_{int} as a Function of the Shear Modulus of the Matrix at Three Volumetric Fractions of the Aluminum Filler (ϕ) and Two Contact Pressures, and d) a Bar-Chart Showing the Increase in Heat Extracted and Decrease in Resistance, for a Meter of Tubing for High (Dark Orange and Dark Blue) and Low (Light Orange and Light Blue) Pressures for Three Experimental Configurations and One ($\phi = 0.3$ of Liquid Metal) Simulated Configuration Indicated by the Star. The Orange Colored Bars Indicate Heat Flux and the Blue the Corresponding Thermal Resistance. the Percentage Increase/Decrease Normalized to the Low Contact Pressure PVC Control Device Is Also Included. 22

2.5 Plot Comparing the Predicted Total Thermal Resistance for Meter of Tubing of the Liquid-Cooled Composite Tubes in Contact with Skin at Low (LP = 0.7 kPa) and High (HP = 6 kPa) Contact Pressures as a Function of the Volumetric Fractions of the Aluminum Filler (ϕ). The Predictions of Segregated Submodels of Tube (R'_{tube}) and Interface (R'_{int}) Resistance for Meter of Tubing Are Also Included. the Green and Purple Shaded Areas Are Used to Highlight the Decrease in Respective Resistances That an Increase from a Low to High Contact Pressure 28

Figure Page

2.6 Plots of a) Mean Outlet Water Temperature ($T_{m,out}$) and b) Total Heat Removed ($\dot{Q}$) as a Function of the Tubes' Length (L_{tube}) for Various R'_{tot} and Low (Laminar Indicated With Light Blue Shade) and High (Turbulent Indicated With Light Orange Shade) Mass Flow Rates, Simulated at a $T_{m,in} = 20\ °C$ and $T_s = 35\ °C$.....30

2.7 Calculated Pressure Loss (ΔP) Per Meter and Pumping Power per Meter of the Tubing as a Function of the Mass Flow Rate, the Vertical Dashed Line Indicates the Flow Rate at Which the Flow Regime Transitions from Laminar to Turbulent. 32

3.1 Illustration (a) and Photograph (b) Of an Example Single-Stream Soft Heat Exchanger; In (b) Only Silicone Was Used to Make the Tube to Make the Extension Spring Embedded in the Tube Wall as Well as Dyed Red Water in the Inner Cavity Visible; (c) Top Row Schematically Shows the Eff of Axial Extension on the Tube Wall, Inner Channel, and the Liquid Metal Micro-Droplets; The Bottom Row Shows the Microscopic View of the Effects of Tube Stretching on the Liquid Metal Droplets. 36

3.2 (a) An Illustration of the Flow Loop That Was Implemented in This Study, (b) the Effect of Stretch-Retraction of the Tube on Its Inner Diameter With a Static Extension, a Slow Actuation Rate Of 0.44 mms^{-1}, and a Fast Actuation Rate of 3.82 mms^{-1}, and (c) The Effect of Stretch-Retraction on the Flow Rate Through the Device. 39

Figure Page

3.3 Representative Demeaned Spring Temperature Over Two Cycles of Extension-Retraction for (a) a Silicone Tube with Highlighting Arrows to Show the Rate Dependent Phase Shift and Amplitude Decay and (b) for a Liquid Metal Composite Tube Consisting of 20% Liquid Metal Volume Fraction. 48

3.4 The Measured and Theoretically Predicted Spring Temperature Phase Shift as a Function of (a) the Device Actuation Time Scale, t_d and (b) The Dimensionless Ratio of the Conductive to Device Actuation Time Scale, t_k/t_d 50

3.5 The Difference Between Peak Average Spring Temperature in Nonactuated (Quasi-Static Like) and Actuated Conditions as a Function of the Corresponding Phase-Shift. 53

CHAPTER 1

1. INTRODUCTION

1.1 Motivation

From building-sized power plant condensers to fingertip-sized microelectronics cooling systems,[2] heat exchangers (HXs) are used to transfer thermal energy in an immense array of applications. Since at least the industrial revolution, these devices have been made of rigid, predominantly metallic materials; as a result, the design knobs that we can manipulate for operational control are limited to the flow temperature and rate. In contrast, in nature there are many elegant systems based on soft materials that effectively move heat and control its transfer rate by dynamically changing shape. For example, based on cooling or heating needs of our own bodies, the capillaries near our skin dilate or constrict.[3] Furthermore, micro scale surface deformations allow soft materials to make better contact with other surfaces due to which there are drastic reductions in thermal resistance brought about by surface roughness. Regardless of the potential benefits of transitioning to a soft material, "soft heat exchangers" (SHXs) are already emerging to enable the continued growth of fields such as thermoregulatory garments, soft robotics, wearable electronics and high powered robotics, all of which require cooling solutions to be soft and deformable. Making such devices has so far been limited by the lack of multifunctional materials with a fitting set of thermo-mechanical properties. Specifically, traditional synthetic soft materials with suitable mechanical properties have a thermal conductivity ($k \approx 0.2$ $Wm^{-1}K^{-1}$) that is too low for most industrial applications.

The lack of effective materials for soft heat exchangers is beginning to be addressed with the recent introduction of elastomer composites with room-temperature liquid metal (LM) fillers.[1,4–6] In contrast to solid particle fillers, LM micro-droplets deform with the elastomer matrix which drastically reduces the negative impacts on a composite's mechanical properties. These materials have shown up to 600% extensibility even with 50% of the composite volume being occupied by liquid metal.[1] At the same time, adding LM increases thermal conductivity up to 2 to 5 $Wm^{-1}K^{-1}$ (for filler volume fraction, ϕ, of 50 to 80%) in an undeformed state and up to 10 $Wm^{-1}K^{-1}$ anisotropically if the material is stretched (with $\phi = 50\%$).[1,5] The numerous recent reports of further improvements in thermal conductivity of LM itself[7,8] and in elastomer-LM composites[5,9–11] achieved through the incorporation of solid particles, indicate that improvements in thermal properties of soft materials are likely to continue. With this enabling technology in mind, in this thesis, I lay the foundations of a framework for the design of such devices.

1.2 Summary and Outline

To simplify the complex nature of studying such a system, I split this work into two sequential steps. First, I explore the effects of transitioning to a soft, surface deformable SHX under steady state static conditions in the setting of liquid cooling in thermoregulatory, electronics, and robotic applications. Second, from a more fundamental perspective, I explore the effects of transient shape deformation during SHX operation.

Thermoregulatory garments composed of liquid-cooled plastic tubes have users ranging from astronauts to multiple sclerosis patients and are emerging as a flexible

cooling solution for wearable electronics and highpower robotics. Despite the plethora of applications, the current cooling systems are cumbersome to use due to their excessive size. In Chapter 2 this issue is resolved by developing soft, thermally conductive silicone–aluminum composite tubes. To achieve optimal device performance, the material must be designed to balance the decrease in bulk thermal resistance and the increase in interfacial tube-substrate resistance due to composite stiffening. Thus, to enable the rational design of such tubes, a closed form, steady state, thermomechanical model that predicts cooling performance as a function of tube geometry and filler fraction is developed and experimentally validated. Predictions via this model and experiments are used to reveal how the tube's geometrical and material design can be adjusted to minimize the required length of tubing and maximize the heat extracted from a metallic surface and skin. Lastly, through a holistic analysis, this work demonstrates that besides significantly increasing overall cooling capability, the use of low-resistance tubing can provide a multifold reduction in the cooling system size and enable novel operating modes.

While in Chapter 2, I am able to encapsulate and predict thermal performance of a SHXs under static deformation, in general the SHXs can undergo large intermittent or periodic deformations during operation. For example, in thermoregulatory garments or soft robotics, there will be actuation and deformation of SHXs caused by the motion of the body and the actuation of the robot, respectively. To begin exploration of this aspect of SHX, in Chapter 3 I use silicone-liquid metal composites to develop single-stream, soft heat exchangers and explore their thermofluidic performance as they undergo large

shape change. The transient device shape change invalidates many conventional assumptions employed in heat exchanger design making analysis of this devices' operation a non-trivial undertaking. To this end, using time scale analysis I demonstrate when the conventional assumptions break down and highlight conditions under which the quasi-static assumption is applicable. In this gradual shape modulation regime traditional fixed-geometry and material property models can be extrapolated in-between time steps to predict the devices thermal performance. I validate this time scale analysis by experimentally characterizing thermo-fluidic performance of our soft heat exchanger as it undergoes axial periodic extension-retraction at varying frequencies during operation. By doing so I explore multiple shape modulation regimes and provide a theoretical foundation to be used in the design of soft heat exchangers undergoing transient deformation. Finally, in Chapter 4, I conclude the two studies by summarizing this work, outlining applications, and discussing potential future work.

CHAPTER 2

2. THERMAL PERFORMANCE OF A STATIC, STEADY STATE, SOFT HEAT EXCHANGER

Liquid Cooled Jackets (LCJ), consisting of garments with a network of rigid Polyvinyl chloride (PVC) tubes cooled by circulating water (see Figure 2.1a), were first used in the 1960s to cool British pilots[12] and then used in the 1970s to cool astronauts during space missions.[12–15] Compared to other thermoregulatory garments,[16,17,26–32,18–25] LCJs are known to provide the highest environment-independent cooling capacities.[15,16,33,34] Thus, unsurprisingly, this concept has been adopted for thermal management of a wide range of users and applications including race-car drivers, surgeons, chemotherapy and multiple sclerosis patients, athletes, as well as hazmat workers[14,19,42–45,20,35–41] and even high-power robotic limbs (see schematics in Figure 2.1).[46–48] Furthermore, with increasing popularity and capabilities of wearable technologies (thus increasing heat generation),[49–54] LCJs will likely be needed to dissipate combined thermal loads from the electronic and the users' body. Despite the plethora of current and emerging applications, the basic LCJ technology has not changed much since its conception. As a result, even with improvements to the tubing network layout, tube cross-sectional geometry, and flow controls,[14,15,21,33,55–59] an upper body LCJ typically consists of around 20 m of PVC tubing, which is rather heavy and cumbersome to wear (a full body LCJ has over 100 m of tubing). To make LCJs more compact, and thus more comfortable to wear or easier to integrate with electronic devices, Flouris and Cheng[33]

recently recommended improving the thermal characteristics of the tubing via material engineering.

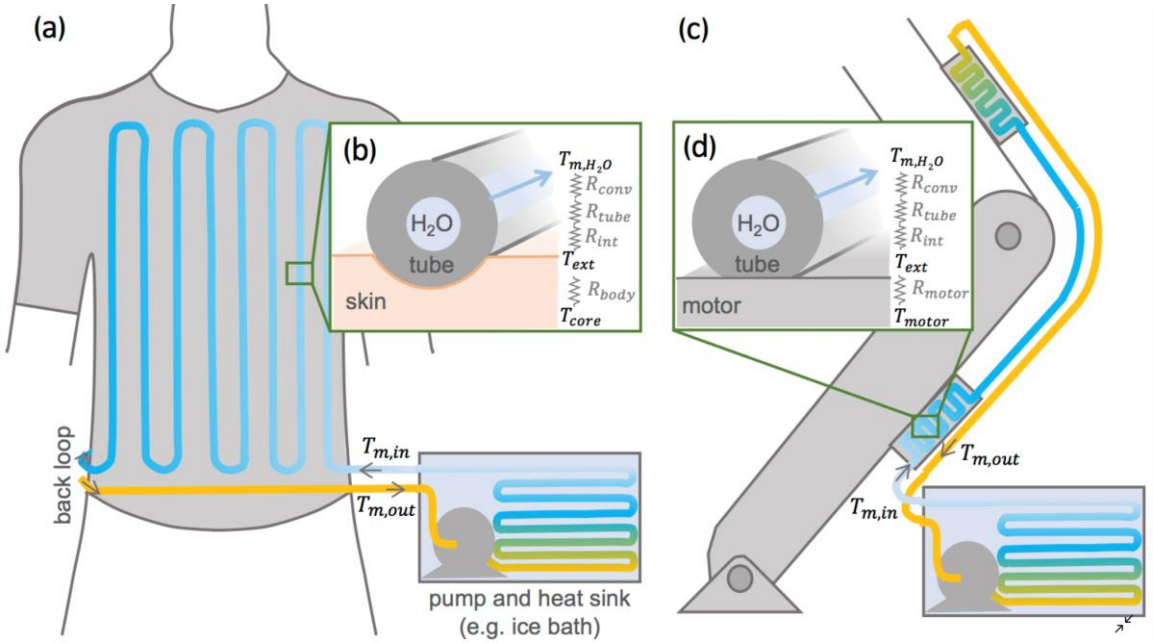

Figure 2.1 Illustrations of a) an upper body liquid-cooled jacket layout, b) a corresponding cross-section of the tube interface with skin (fabric is assumed to be located on outer part of the tube), c) liquid-cooled jacket used to cool motors within a robotic leg, and d) a corresponding cross-section of the tube interface with the motor. T_{m,H_2O}, $T_{m,in}$, $T_{m,out}$ stand for mean, mean inlet, and mean outlet water temperatures, and R_{conv}, R_{tube}, R_{int}, R_{body} and R_{motor} stand for convective, tube, interface, body, and motor thermal resistances, respectively.

The rate of heat removed by tube pressed against a surface, either skin or metal, can be estimated using a thermal resistance network, where the total thermal resistance (R_{tot}) is the sum of resistances posed by the internal convection of water (R_{conv}), the conduction through the tube wall (R_{tube}), and the tube wall-substrate interfacial resistance (R_{int}). Calculations presented in Appendix A show that for a rigid 1 m long PVC tube, $R'_{tube} \approx 1$ m°CW^{-1}, $R'_{int} \approx 0.3$ to 1.6 m°CW^{-1}, and, depending on the flow regime, $R'_{conv} \approx 0.01$ to 0.3 m°CW^{-1} (apostrophe refers to resistance for one meter of

tubing). Consequently, in this work I study how tubing made of soft, thermally conductive elastomeric composites can reduce the dominant resistances, R'_{tube} and R'_{int}; thus reducing the amount of necessary tubing while increasing the capacity for heat extraction.

R'_{tube} can be reduced by increasing the thermal conductivity of the polymer tube material, which can be accomplished through the addition of conductive fillers. In fact, many groups have demonstrated heat exchangers that consists of "hard" polymer composites.[60–62] However, the addition of filler particles tends to stiffen elastomers,[63,64] which counterproductively increases R'_{int},[65–69] reduces the wearability and makes the composite prone to cracking under common operating conditions. Thus, designing of tubing made of a composite requires balancing the desired mechanical and thermal properties, where both are controlled by a variety of factors such as, filler fraction (ϕ), type of filler particle, elastomer matrix, interface roughness, type of substrate being cooled, etc. To enable rational design of such soft composite tubing, I develop a closed-form thermomechanical model that predicts their cooling performance as a function of their geometry, the contact surface, material properties, and filler fraction in the composite. To do so, I first prepare silicone-aluminum particle composites, characterize their relevant thermal and mechanical properties and match them with predictive sub-models available in literature. To validate the full model that combines the material and thermal resistance sub-models, I fabricate devices consisting of tubing made out of the silicone-aluminum composites and measure their performance using a custom setup. I reveal the nuances and differences of applying the full thermomechanical model to

personal (skin) and robotic (metal) cooling and, using a combination of predictions utilizing this model and experimentations, I explore strategies for improving the cooling capability on such surfaces. Finally, I demonstrate to what extent using composite material tubing would help and carry out a holistic discussion including design factors such as, effect of geometry, flow rate and pumping power.

2.1 Experimental Section

2.1.1 The Composite Tube Fabrication

The composites were fabricated by dispersing aluminum powder (Alfa Aesar, see Appendix A) in a two-component silicone (SmoothOn, Smooth-Sil 960). Specifically, I mixed the aluminum powder into part A of the silicone and then used a high-speed mixer (Dremel 3000) to ensure even dispersion. For high filler densities, I added 2% silicone thinner by volume (SmoothOn) for easy and uniform mixing of the highly viscous mixture. I then added the part B of the silicone (cross linker) and further mixed the components using a high-speed mixer. The final mixture was then degassed in a vacuum chamber to remove any air bubbles. The resulting silicone was cast into a custom mold as seen in Figure 2.2a. Each cast device had a total volume of 150 mL, where the bottom 100 mL consisted of this thermally conductive silicone-aluminum composite and the top 50 mL consisted of silicone without filler (see Figure 2.2d). To achieve the layering, I simply poured the two mixtures in series. The entire final mold was then once again vacuum degassed and cured at 20 °C for 16 hours. Figure 2.2 illustrates this process and the mold, which was machined out of an acrylic plate.

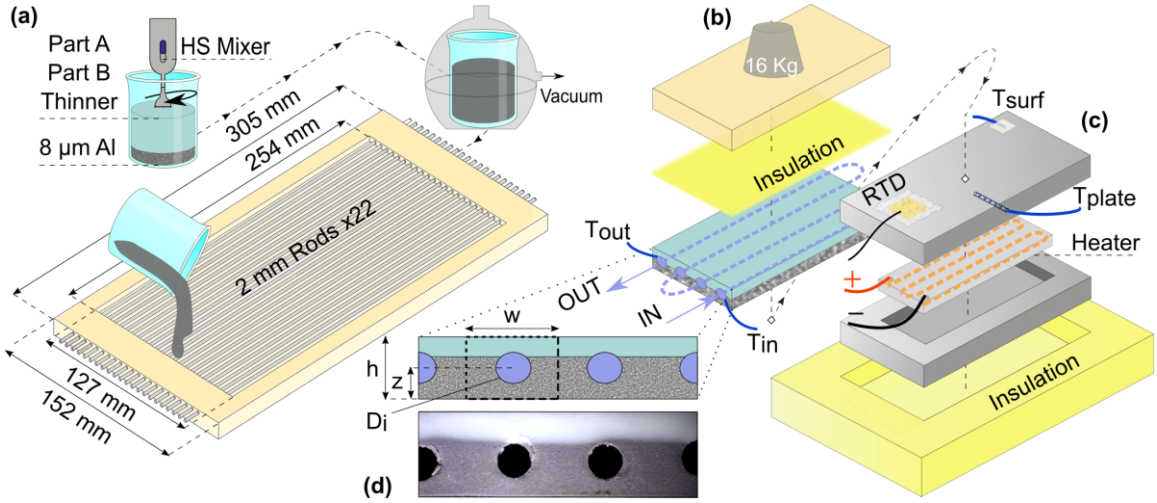

Figure 2.2 Illustrations of a) the casting procedure and the dimensions of the mold, the exploded view of b) the experimental setup and c) the hotplate configuration with sensor placements indicated, d) photograph and schematic cross-sectional view of the device, with indicated dimensions ($h = 4\ mm$, $z = 2\ mm$, $D_i = 2\ mm$ and $w = 5.5\ mm$).

I fabricated the mold by end milling 4 mm deep into a 12.7 mm acrylic and drilling an array of holes on the two ends, where, the holes were used to align and suspend twenty-two steel rods with 2 mm diameters across the mold. The rods were placed centrally, so that that there was a 1 mm thick wall on the bottom and the top of the casted channels. Prior to casting, I cleaned the mold and the steel rods using isopropyl alcohol to remove dirt and uncured silicone and coated them with EaseRelease® 200 to facilitate the detachment of the cast device. Upon curing, the embedded steel rods were pulled out, forming a series of channels. The channels were connected to each other via PVC tubing (McMaster-Carr, D_i = 2.38 mm, D_o = 3.96 mm) and complimentary barbed connectors (McMaster-Carr) to form a continuous serpentine channel. Using the same PVC tubing I fabricated a control device and using the above procedure but varying the

filler fraction, I fabricated devices with aluminum filler volume fraction, ϕ, of 0, 0.1, 0.2 and 0.3.

2.1.2 Measurement of the Cooling Capability of the Composite Tubes

To measure the thermal performance of the tubes, I developed a hotplate setup adhering to recommendations by Cao and co-workers for testing of thermoregulatory LCJ.[70] Specifically, I embedded a 7.6 cm by 30.5 cm 110 V alternating current strip heater (McMaster-Carr, part #3619K852) in a grooved 12.7 cm by x 30.5 cm aluminum plate and covered this assembly with another aluminum plate of equivalent dimensions. To control the surface temperature of the plate, I connected the heater and an embedded surface RTD (Omega, Pt-100 Class A) to a PID controller (Omega, CSi8D) that was capable of maintaining a temperature to +/-0.05°C. Care was taken to keep the plate surface flat by embedding the RTD into a machined groove and covering it with epoxy. I also embedded two additional thermocouples (Omega, T-type), one on the surface and another in the central groove as shown in Figure 2.2c. To prevent heat loss, I insulated the heater assembly with a thick layer of insulating foam (Great Stuff window and door insulating foam). Lastly, the surface of the hotplate was polished using a 600-grit sandpaper and cleaned with isopropyl alcohol prior to each test.

Using the above setup, I measured the total resistance for unit length of each device at a low and high contact pressure. The devices were secured flat using thin double-sided tape on either ends of the device. Thermocouples (Omega, T-type) were inserted into the inlet and outlet PVC tubing to measure the respective temperatures. On top of the device, I placed a 2 mm thick insulation layer (Pyrogel, #PG2250-1226), a 1.5

kg acrylic plate, and, for high contact pressure experiments, an additional 16 kg weight (see Figure 2.2b). The experiments were initiated by running water at 150 mL min^{-1} through the device using a peristaltic pump (Omegaflex™ Peristaltic Pump, FPU500-FPU5MT). To further reduce potential of any heat transfer from the ambient, I maintained the inlet water temperature at 20°C using a refrigerated water bath (VWR, Cat #89203-014). Once steady flow of water was established, I turned on and set the PID-controlled hot plate to a surface temperature of 35°C, which was chosen to emulate body temperature. Note that our results are presented in terms of thermal resistance, consequently, should be independent of the surface-cooling liquid temperature difference, at least within the plausible working temperature range of 10 – 50°C for the cooling jacket. However, at relatively extreme values of temperatures (e.g. below 0 or above 100 °C), there may be additional consideration, such as the polymer matrix stiffening, softening, or deterioration that are not considered in this work. Once the water outlet temperature fluctuation reduced to, at most, +/- 0.05 °C, steady state was reached and I collected inlet, outlet and two plate temperatures for 15 minutes using a data acquisition system (Stanford Research Systems, PTC10). I corrected the raw data using a calibration curve (see Appendix A) and averaged each temperature data set over time. I calculated the total heat transfer rate to the cooling device, $\dot{Q}$, as:[71]

$$\dot{Q} = \dot{m} c_p (T_{m,out} - T_{m,in}) \tag{2.1}$$

Where $\dot{m}$ is the flow rate, which is set to 2.5×10^{-6} m^3 s^{-1} (150 ml min^{-1}), $T_{m,in}$ and $T_{m,out}$ are the mean inlet and outlet water temperatures and c_p is the specific heat taken as 4184 $Jkg^{-1}°C^{-1}$.[71] Since the thermal gradient within our devices in the vertical direction

($\Delta T_z/\Delta z \approx 15/0.1 \approx 150$ °C cm^{-1}) is much greater than in horizontal direction ($\Delta T_x/\Delta x \approx (4/20)/0.55 \approx 0.36$ °C cm^{-1}), I assumed that the tubes are thermally isolated from each other. Thus, the total resistance for unit length, R'_{tot} (units of m°CW^{-1}), can be calculated as:

$$R'_{tot} = \frac{\Delta T_{LM} L_{tube}}{\dot{Q}} \tag{2.2}$$

Where ΔT_{LM} is the log mean temperature difference, which is defined as:[71]

$$\Delta T_{LM} = \frac{(\Delta T_{out} - \Delta T_{in})}{ln\left(\frac{\Delta T_{out}}{\Delta T_{in}}\right)} \tag{2.3}$$

Where $\Delta T_{in} = T_s - T_{m,in}$, $\Delta T_{out} = T_s - T_{m,out}$, and T_s is the temperature of the hot plate. It is worthwhile to note that in our experiments the difference between ΔT_{in} and ΔT_{out} was less than 40% and thus, the error of taking the arithmetic average as opposed to the log mean temperature difference, would have been less than 1% (i.e. $\Delta T_{LM} \approx T_s - (T_{in} + T_{out})/2$).[71] Furthermore, an error propagation was carried out using the Taylor Series Method to evaluate the standard uncertainty of the measured total resistance readings and thus, the results are presented with a 95% confidence interval error bar (See Appendix A).

2.1.3 Mechanical Characterization of the Silicone Composites

I found that there were two mechanical characteristics relevant to this analysis, the Young's Modulus used as a measure of the wearability and the shear modulus used in modeling the interface resistance. To measure the former, I cast 50% dimensions of type C dog bone samples of the composites for tensile testing following the guidelines of ASTM-D412. The tests were performed on an Instron 5942 with a 50 N load cell up to

10% strain at a rate of 1 mm s^{-1}, followed by relaxation to capture any loss of stiffness or increase in strain hysteresis (see Appendix A Section 4). The stress and strain was calculated as F/A and as $\Delta L/L_o$ respectively, where F is the applied force, A is the average cross sectional area of the sample (measured at three locations), ΔL is the extension and L_o is the length of the sample test section. In addition, I also measured the ultimate strength of the composites by stretching one of the samples of each filler fraction that were tested to failure (see Appendix A Section 4). Note that all our dog-bone samples stretched without failure beyond 30% (see Appendix A Section 4), indicating compatibility with wearable application.

To measure the shear modulus of the polymer composites, I performed small amplitude oscillating shear tests on a rheometer (DHR-2, TA instruments). I tested 1.3±0.2 mm thick samples in a parallel plate configuration of 25 mm size and repeated the test for four samples per filler configuration. At 1 rad s^{-1} frequency, I first performed a strain sweep by varying the strain from 0.01-10% to determine the linear viscoelastic region (LVR). I observed the storage modulus dropping gradually after 1% strain, indicating the end of LVR. The modulus values I report are at 0.1% strain and 1 rad s^{-1} frequency since the measured values were observed to be fairly constant over the entire range of LVR (see Appendix A).

2.1.4 Thermal Characterization of the Silicone Composites

I measured the thermal conductivity of the composites using a Hot Disk Thermal Constants Analyzer (Thermtest,TPS2500S). To satisfy the infinite sample assumption underlying this method, it is recommended that the thermal wave probing depth be

smaller than the smallest sample size, calculated as $\Delta_p = 2\sqrt{\alpha t}$, where α is thermal diffusivity of the sample and t is time of the experiment. Based on previous experiments, I estimated that for our composites the maximum $\Delta_p \approx 6$ mm.[9] Consequently, I made 10 mm thick disks with 25 mm diameter. I fabricated and tested three sets of samples for each filler fraction. I carried out the measurements using sensor design 5465 (3.2 mm radius Kapton sensor), with a measuring time of 20 s and a heat flux of 50 mW. In this test method, the heat sensor is used as both a heat source and a temperature sensor and thus measures both the heat input, output and the temperature increase in the sensor. The thermal conductivity values measured via this method have a manufacture specified accuracy of ±5%.

2.1.5 Sample Imaging Procedures

To measure the surface roughness, I imaged the morphology of the active surface of the hot-plate and all the LCJs using a high magnification optical profilometer (Zygo ZeScope) with an objective lens of 5x. To obtain representative data sets, I imaged long strips (1.38 mm x 45.17 mm) that consisted 240 stitched individual images with 10% overlap between images across each sample. Subsequently, I extracted line profiles of the surfaces, which were used to calculate the root-mean square (RMS) roughness, see Appendix A for example line scans. To characterize the filler particles, I drop casted the aluminum powder on a silicon wafer and imaged this sample using an Amray 1910 scanning electron microscopy (SEM) with a field emission gun, accelerating voltage of 20 kV and beam spot setting of -26. I subsequently used ImageJ to analyze the images and quantified the particle size distribution that is presented in the Appendix A.

2.2 Results and Discussion

2.2.1 Composite Models and Measured Properties

To formulate the closed form thermomechanical model of the tubes thermal resistance, I need to be able to model the relevant material properties as a function of the composite composition. As such, in this section I prepare silicone-aluminum particle composites, characterized their relevant properties and match them with predictive material sub-models available in literature. In particular, I focus on the thermal conductivity (k_c), shear modulus (G_c), and surface roughness (σ) of the composites which are used in R'_{tube} and R'_{int} sub-models. In addition, I also study Young's modulus (E_c) which is helpful in assessing the wearability of the cooling device. As expected, the plots in Figure 2.3 shows that an increase in the aluminum filler fraction results in an increase in each of the material properties in consideration.

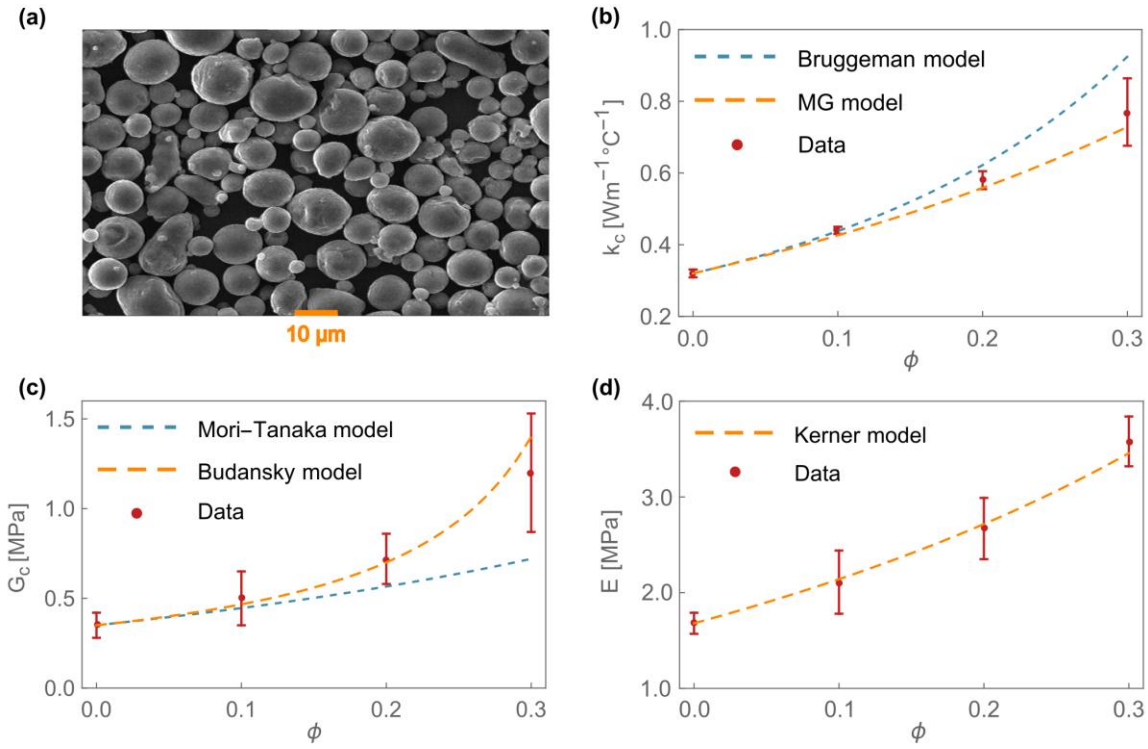

Figure 2.3 a) Representative SEM image of the aluminum particles; plots of the measured composite b) thermal conductivity (k_c), c) shear modulus (G_c), d) and Young's modulus (E_c) as a function of volumetric filler content ϕ compared against the corresponding theoretical model.

Concerning thermal conductivity of the composite, according to the Maxwell-Garnett model it can be calculated as:[72]

$$k_c(\phi) = k_m\left(1 + \frac{3\phi(\delta-1)}{2+\delta-\phi(\delta-1)}\right) \tag{2.4}$$

Where $\delta = k_p/k_m$ while k_p and k_m are the thermal conductivities of the filler particles and the elastomer matrix, respectively. Alternatively, the Bruggeman model predicts k_c as:[5,72]

$$1 - \phi = \left(\frac{k_p - k_c}{k_p - k_m}\right)\left(\frac{k_m}{k_c}\right)^L \tag{2.5}$$

Where L is the depolarization factor, which is equal to 1/3 for spherical particles. The plot in Figure 2.3b shows that both models are in good agreement with measured thermal conductivity data for $\phi \leq 0.1$, however, beyond $\phi \geq 0.2$ Maxwell-Garnett provides a better fit. Consequently, I utilize the simple closed-form Maxwell-Garnett formula in our device model. However, I note that for $\phi \geq 0.3$, which is beyond the scope of our current work, the Bruggeman or the Tavangar[9] models typically provide a better match to experimental data than the Maxwell-Garnett model.

In regards to the shear modulus of the composite, the "self-consistent scheme" Budansky model predicts it as:[73,74]

$$G_c(\phi) = \frac{G_m}{1-2.5\phi} \tag{2.6}$$

Where G_m is the shear modulus of the matrix. Alternatively, the Mori-Tanaka model obtained using micromechanics predicts the G_c as:[75]

$$G_c(\phi) = G_m + \frac{\phi G_m(G_p - G_m)}{G_m + \beta(1-\phi)(G_p - G_m)} \tag{2.7}$$

Where G_p is the shear modulus of the filler particle, $\beta = 2(4 - v_m)/15(1 - v_m)$, and $v_m = 0.49$ is the Poisson's ratio of the silicone matrix. The plot in Figure 2.3c shows that the Budansky model provides a much better fit for our data than the Mori-Tanaka model. However, caution should be taken in using the simpler Budansky model for $\phi \geq 0.3$, since the predicted value becomes unbound when $\phi = 0.4$. Since our focus is on composites with $\phi \leq 0.3$, I implement the Budansky formula in our thermomechanical tube resistance model.

To predict the Young's modulus of the composite, the Kerner's model predicts the Young's modulus of the composite as:[75,76]

$$E_c(\phi) = E_m\left(1 + \frac{\phi}{1-\phi}\frac{15(1-v_m)}{(8-10v_m)}\right) \tag{2.8}$$

Figure 2.3d shows how the Kerner model is in good agreement with our measured data, and thus applicable for our purposes.

Lastly, although the average surface roughness, σ_{c-a}, and root-mean-square surface roughness, σ_{c-RMS}, were mostly dictated by the machined surface finish of the acrylic mold, I did measure a mild increase to the range of 10 to 15 µm with volumetric filler content for both parameters (see Figure A2 in Appendix A). As such, in an attempt to model this increase, I found that the dependence of both σ_{c-a} and σ_{c-RMS} on ϕ can be reasonably well predicted using geometric scaling models, which are derived and compared against measured data in the Appendix A. The RMS roughness, which will be used in the thermomechanical device model, was derived and validated to be:

$$\sigma_{c-RMS}(\phi) \approx \sigma_{c-RMS}(0)\left(1 + 0.5\phi^{\frac{1}{3}}\right) \tag{2.9}$$

2.2.2 Thermomechanical Model of Tube's Thermal Resistance and its Validation

In this section, I develop the steady-state thermomechanical model of R'_{tot} which comprises of the three resistances (also illustrated in Figure 2.1):

$$R'_{tot}(\phi) = R'_{tube}(\phi) + R'_{int}(\phi) + R'_{conv} \tag{2.10}$$

Out of these three resistances, R'_{conv} does not depend on ϕ and contributes the least, thus as an approximation it can be neglected (see discussion in Appendix A). Consequently, I focus on developing sub-models of R'_{tube} and R'_{int} as a function of ϕ.

First, by comparing a closed-form analytical solution to a finite element model (FEM) simulation, I find that $R'_{tube}(\phi)$ can be accurately modelled using a simple shape factor approach.[71] Specifically, once a shape factor for meter length of the tube, S', is obtained, the resistance of the tube is simply calculated as:

$$R'_{tube}(\phi) = \frac{1}{k_c(\phi)S'} \tag{2.11}$$

The results from using the shape factor formula for a horizontal cylinder of length L_{tube} midway between two parallel plates of equal length and infinite width ($S_{finite} = \pi L_{tube}/ln(8z/\pi D_i)$ was compared with FEM simulations in Figure A7. Specifically, our results show that R'_{tube} calculated using this shape factor agrees exactly with simulation results for w = 5.5 mm (our device geometry). Since the utilized shape factor was derived for a finite thickness plate of infinite width, exact agreement between analytical and simulated values, with w = 5.5 mm, suggest that heat transfer across the tube will not increase any further through increase of its width. Consequently, for a 2 mm channel diameter and a unit width of 5.5 mm or greater, the unit width does not have to be explicitly taken into account in the resistance calculations. Furthermore, despite the actual and FEM-simulated devices consisting of an insulating top and conducting bottom layers, the results show that utilizing only $k_c(\phi)$ (calculated using Equation 2.4) is sufficient to accurately calculate the thermal resistance of the tube with Equation 2.11.

Next, I focus on developing the sub-model for the R'_{int} as a function of ϕ. To do so, I adopt the model proposed by Prasher and Matayabas[67] and incorporate into it the volumetric filler content of filler particles. Prasher and Matayabas developed their formula by fitting thermal contact resistance data collected for interfaces between

polished metal and soft silicone gels with effective shear moduli ranging from 1 to 460 kPa. Based on this model, $R'_{int}(\phi)$ for meter of contact between the soft silicone tube (material 1) and a hard, relatively much higher thermally conductive material (material 2), can be calculated as:[67–69]

$$R'_{int}(\phi) = 83.8 \frac{\sigma_{s-RMS}(\phi)}{0.5k_s(\phi)} \left(\frac{G(\phi)}{P}\right)^{\frac{1}{4}} \frac{L_c}{wL_{tube}} \quad (2.12)$$

Where P is applied contact pressure, G is the shear modulus of the softer material, $k_s = 2k_1k_2/(k_1+k_2)$ which is the harmonic mean of the thermal conductivities of the two materials in contact, and $\sigma_{s-RMS} = (\sigma_{1-RMS}^2 + \sigma_{2-RMS}^2)^{0.5}$ which is the representative interface roughness. To adopt the Prasher and Matayabas[67] correlation for our discussion, I divided the original formula by the total contact area (wL_{tube}) and multiplied by $L_c = 1$ m. In addition, when contacting with a smooth metallic substrate with a much higher thermal conductivity than that of the composite, two simplifications can be made: $k_s \approx 2k_c(\phi)$ and $\sigma_{s-RMS} \approx \sigma_{c-RMS}(\phi)$. Thus, the final expression for $R'_{int}(\phi)$ for tubing-metal substrate contact (i.e. robotic cooling case) is obtained by substituting expressions for Equation 2.4 for $k_c(\phi)$, Equation 2.6 for $G_c(\phi)$, and Equation 2.9 for $\sigma_{c-RMS}(\phi)$ (see fully expanded expression in Appendix A). In turn, to calculate $R'_{int}(\phi)$ for tube-skin contact, it can be safely assumed that skin will always be the softer material because it has a low frequency shear modulus of only 0.4 kPa.[77] Furthermore, although likely to vary across the body, skin has surface roughness of $\sigma_{skin-RMS} \approx 20$ µm, which, is much higher than a smooth metallic substrate and so $\sigma_{s-RMS} = (\sigma_{c-RMS}^2 + \sigma_{skin-RMS}^2)^{0.5}$. Note that Rykaczewski[69] recently showed that for finger-object contact, Equation 2.12 provides quantitative prediction when substrate conductivity is at least three-fold higher

than that of the skin. Since thermal conductivity of skin, $k_{skin} \approx 0.37$ $Wm^{-1}°C^{-1}$ is within the $k_c(\phi)$ range,[69] Equation 2.12 will only provide an approximate estimate of the $R'_{int}(\phi)$ for tube-skin contact (see fully expanded expression in Appendix A). Finally, by substituting in equation 2.11 and 2.12 into equation 2.10 I form the closed form thermomechanical model for evaluating the total thermal resistance of the composite tubes.

To validate the full thermomechanical model for $R'_{tot}(\phi)$, I fabricated devices with about 5 m of thermally active tubing with rectangular cross-section with varying filler fraction and tested the cooling capability of the devices by flowing water at 150 mL min^{-1} with an inlet temperature of 20°C through the channel while the device was in contact with an aluminum plate whose surface was maintained at temperature of 35°C. I quantified the heat removed by the devices by measuring the mean outlet temperature of the water. This experimental approach is based on the standard method proposed by Cao et al.[70] for testing cooling performance of liquid-cooled garments used for human thermoregulation. Lastly, I simulated poor and good contact of the devices with the substrate by applying low ($P \approx 0.7$ kPa) and high ($P \approx 6$ kPa) contact pressure during the experiments (see details in the Experimental Section). The plots in Figure 2.4a and 2.4b show that the resistance values I measured agree well with our model over the entire ϕ range for both tested contact pressures.

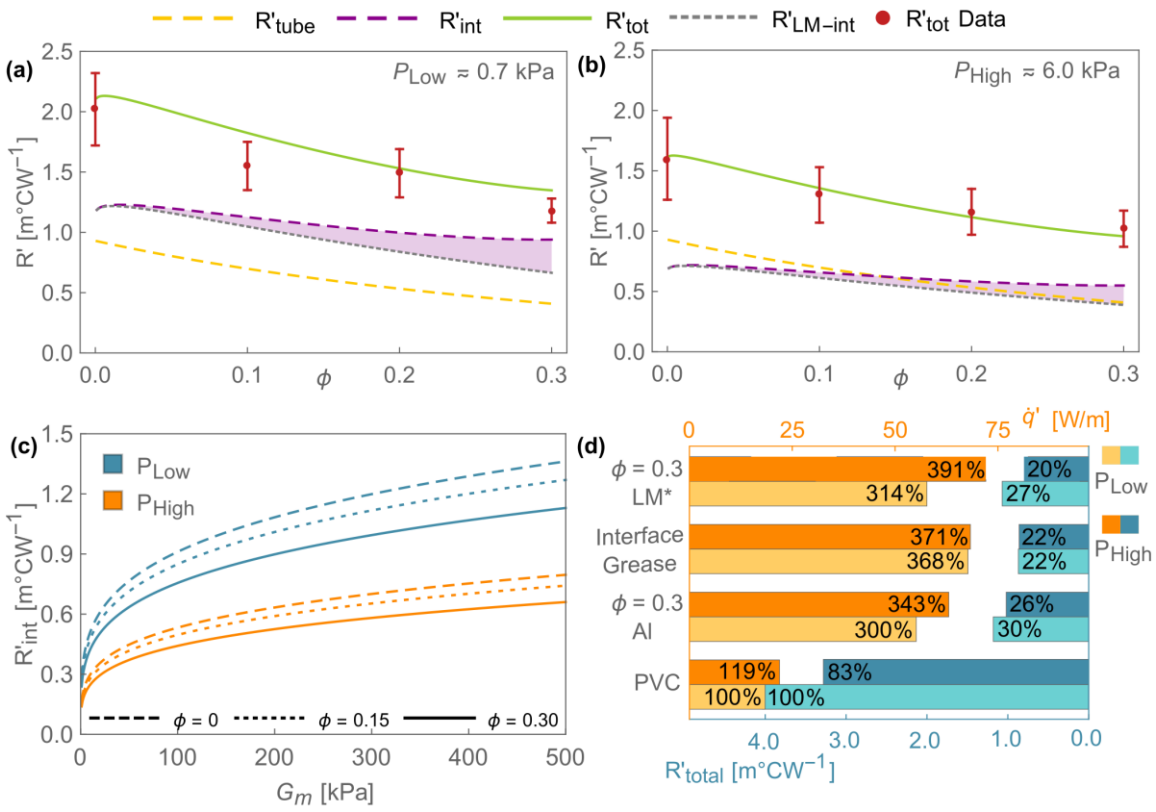

Figure 2.4 Plots comparing the measured and predicted total thermal resistance for meter of tubing of the liquid-cooled devices in contact with the hotplate at a) low and b) high contact pressure. The predictions of the submodels of tube (R'_{tube}), interface (R'_{int}), and interface with liquid metal filler are also included (R'_{LM-int}) as indicated by the diverging purple shaded area. c) The variation of R'_{int} as a function of the shear modulus of the matrix at three volumetric fractions of the aluminum filler (ϕ) and two contact pressures, and d) a bar-chart showing the increase in heat extracted and decrease in resistance, for a meter of tubing for high (dark orange and dark blue) and low (light orange and light blue) pressures for three experimental configurations and one ($\phi = 0.3$ of liquid metal) simulated configuration indicated by the star. The orange colored bars indicate heat flux and the blue the corresponding thermal resistance. The percentage increase/decrease normalized to the low contact pressure PVC control device is also included.

2.2.3 Strategies for Improving Cooling Capability of Tubes in Contact with Metallic Substrates

In all of the experiments R'_{tot} varies between 1 and 2 m°CW^{-1}, gradually dropping by about 0.6 to 0.7 m°CW^{-1} through the addition of alumina particles. Specifically, at low

contact pressure R'_{tot} decreases from 2.0 m°CW^{-1} to 1.2 m°CW^{-1} and at high contact pressure the R'_{tot} decreases from 1.6 m°CW^{-1} to 1.0 m°CW^{-1}. In contrast, the control device consisting of round PVC tubing had a R'_{tot} of 4.0 m°CW^{-1} and 3.3 m°CW^{-1} at low and high contract pressure, respectively, even though its tubing had a thinner wall (0.79 mm vs. 1 mm for silicone). In other words, switching the cross-sectional geometry from round to rectangular and the material from PVC to a silicone-aluminum composite of ϕ = 0.3 reduces the resistance of the device to 26 – 30 % of the control, and with that increases the heat transfer rate to 300 – 343 % (see Figure 2.4d). Based on additional FEM simulation, I estimate that a pipe with the same rectangular contour as our devices but made from PVC ($k_m = 0.17$ Wm^{-1}°C^{-1}) has R'_{tube} of 1.8 m°CW^{-1}. Consequently, the majority of the reduction in R'_{tot} is due to the change in external tube geometry from circular to rectangular (exact quantification attributed to this change is difficult since exact contact area of the circular tubes with the substrate is unknown and difficult to predict). To highlight the importance of even a minor change in the device thermal conductivity at low values, note that just by switching the matrix material from PVC to the silicone ($k_m \approx 0.3$ Wm^{-1}°C^{-1}) the R'_{tube} of the rectangular contour device reduced substantially from 1.8 m°CW^{-1} to about 1.0 m°CW^{-1}. In fact, liquid-cooled silicone head caps with comparable rectangular contours have been used commercially for a few years in localized scalp cooling, which helps to prevent patient hair loss caused by chemotherapy.[21] This cooling therapy is administered in clinics and so portability of the cooling device is not a major concern. However, commercial use of silicone tubing with rectangular geometry signals that such transition is feasible for LCJs, and as our results

show, this would enhance cooling. Also note that thermal resistance of the rectangular contour tube could be further decreased by thinning the walls.[15,58] However, this approach decreases durability and increases risk of damage and leakage. Additionally, thinner walls lead to tube inflation and thus higher contact resistance (see Appendix A).

The segregated sub-model plots in Figure 2.4 show that the $R'_{tube}(\phi)$ decreases significantly while $R'_{int}(\phi)$ decreases only mildly as ϕ increases. Consequently, the 0.8 to 0.6 m°CW^{-1} decrease in R'_{tot} with increasing aluminum content predominantly stems from the increase of the composite thermal conductivity from 0.3 to 0.7 Wm^{-1}°C^{-1} (see Figures 2.3b and 2.4a-b). From an optimization standpoint, it is important to point out that further increasing k_c beyond the 0.7 Wm^{-1}°C^{-1} achieved with ϕ =0.3 (see Figure 2.3b) will provide diminishing returns in reducing R'_{tube}. Specifically, while the increase of k_c from 0.3 to 0.7 Wm^{-1}°C^{-1} resulted in a tube resistance decrease of at least 0.6 m°CW^{-1}, further increase of k_c of equal magnitude from 0.7 to 1.1 Wm^{-1}°C^{-1} would only decrease the tube resistance by 0.15 m°CW^{-1}. Additionally, such an increase would result in increased stiffness, device weight and cost, as such it is not a worthwhile path to improve LCJ performance. It is also useful to mention that by exploring the Maxwell-Garnett model (Equation 2.4) and previous literature,[9] it can be established that increasing the particle thermal conductivity beyond about 20 Wm^{-1}°C^{-1} has very little impact on k_c. In other words, it is not worthwhile switching the filler from aluminum to a material with higher conductivity such as copper. In turn, switching from aluminum to materials with lower thermal conductivity of around 20 Wm^{-1}°C^{-1} such as aluminum oxide, titanium, or gallium-based liquid metals[71] would also not affect the device

performance, but could have some other benefits (e.g. lower cost or weight). In contrast, k_c increases linearly with increase in the matrix thermal conductivity, consequently selecting a more conductive silicone provides a significant improvement in the tube's cooling capability (as highlighted above with switch from PVC to silicone).

From Equation 2.12 and associated material models, we can infer that $R'_{int}(\phi)$ changed only mildly as ϕ increased (from 1.2 to 0.94 m°CW^{-1} at low contact pressure and from 0.69 to 0.54 m°CW^{-1} at high contact pressure). From the model we can infer that this mild change was caused by the benefits of increasing k_c being offset by the drawbacks of increasing $\sigma_{s-RMS}(\phi)$ and $G(\phi)$. Minimizing surface roughness should always be recommended but it might not be feasible for cost or manufacturing reasons. However, increase in $G(\phi)$ could be easily mitigated by either switching the solid filler to microscale liquid metal droplets or by using a softer matrix. The former approach is based on recent work by Bartlett et al.,[5,78] who demonstrated that adding even up to ϕ = 0.5 of room-temperature liquid metal (eutectic GaIn or GaInSn) micro-droplets to a silicone increases thermal conductivity (comparable to the addition of aluminum particles of same size) but does not appreciably change mechanical properties of the composite. To quantify the benefits of solid to liquid metal filler switch, I calculate $R'_{int}(\phi)$ for shear modulus kept constant at the value corresponding to ϕ = 0 for all values of ϕ. The gray dotted lines (diverging from the purple line) in the plots in Figures 2.4a-b show that addition of $\phi = 0.3$ of liquid metal instead of aluminum would reduce $R'_{int}(\phi)$ from 1.2 to 0.68 m°CW^{-1} (vs. 0.94 m°CW^{-1} for aluminum, see the filled in purple area in Figure 2.4a at low contact pressure and from 0.69 to 0.38 m°CW^{-1} (vs. 0.54

m°CW^{-1}, see the filled in purple area in Figure 2.4b at high contact pressure. Consequently, switching the filler type from solid to liquid could yield a further 3 – 6 % reduction in total resistance below the reduction achieved from PVC device by using silicone-aluminum tube with ϕ = 0.3 (see Figure 2.4d). However, we also need to take into consideration that gallium based alloys are corrosive, dense, and comparatively expensive, as such their application to wearable cooling devices and other applications requires careful real-life testing.

To quantify the benefits that could be attained using a softer matrix, I used our model to estimate R'_{int} for six combinations of filler content and applied pressure (ϕ of 0, 0.15, and 0.3 and P of 0.7 and 6.0 kPa) with matrix shear modulus varied between 0.1 and 500 kPa. Figure 2.4c reveals that the biggest benefits would be attained at the lowest contact pressure, where decreasing the shear modulus of the matrix from the current 330 kPa to 100 kPa would decrease the R'_{int} by about 0.2 m°CW^{-1}. However, I found softening the entire matrix leads to reduced mechanical durability and, I speculate, it will also lead to a significant increase in the interface resistance due to the inflation of tubes under the transmural pressure difference (see discussion in Appendix A Section 8). Moreover, Figure 2.4c also shows that a truly substantial decrease in contact resistance at all contact pressures could only be achieved by switching to an extremely soft matrix material with shear modulus below 5 to 10 kPa. Though reducing the modulus of the entire tubing material to such depths is not practical, incorporation of a very thin soft layer at the bottom of the device is feasible. To quantify the extent such a device could improve the performance, I carried out two additional experiments. I fabricated silicone

devices similar to previous ones with ϕ of 0.3, but with an additional thin soft silicone bottom layer of about 50 μm (SmoothOn EcoFlex 00-10 with $G_m \approx 18$ kPa). While the introduction of such a thin layer should theoretically increase the tube resistance minimally by about 0.025 m°CW^{-1}, I measured R'_{tot} of 0.97 m°CW^{-1}, which is comparable to that of the same device without the additional layer. This lack of decrease in the total resistances could stem from fabrication imperfections, the model not capturing micromechanics of layered materials, or from the introduction of an additional interface contact resistance in-between the two silicone layers. To circumvent these complications and still capture the potential decrease in total resistance, I added uncured Sil 960 Part A in the interface to act as a thermal interface material. This experiment resulted in a decrease in R'_{tot} to 0.79 m°CW^{-1} at both high and low pressure, demonstrating the contact resistance cannot be reduced much further. Showing that this approach has some viability, this value of R'_{tot} corresponds to a further 4 - 8 % decrease of total resistance below reduction achieved from PVC device by using silicone-aluminum tube with ϕ = 0.3 (see Figure 2.4d).

2.2.4 Model Based Strategies for Improving Cooling Capability of Tubes in Contact with Skin

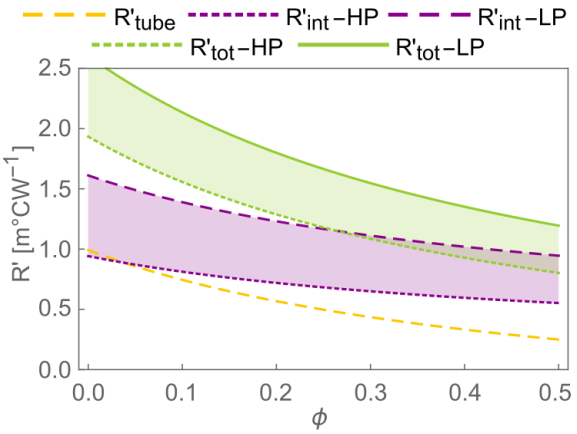

Figure 2.5 Plot comparing the predicted total thermal resistance for meter of tubing of the liquid-cooled composite tubes in contact with skin at low (LP = 0.7 kPa) and high (HP = 6 kPa) contact pressures as a function of the volumetric fractions of the aluminum filler (ϕ). The predictions of segregated submodels of tube (R'_{tube}) and interface (R'_{int}) resistance for meter of tubing are also included. The green and purple shaded areas are used to highlight the decrease in respective resistances that an increase from a low to high contact pressure achieves.

In this section I use the R'_{tot} model to explore how composite tubes could be optimized for thermoregulation. Note that the discussed resistance values should be treated as rough estimates due to uncertainties stemming from the above-mentioned caveats of using Equation 2.12 for modeling of skin contact resistance.[69] In all, the model suggests that the R'_{tot} can be decreased by reducing R'_{tube} via geometry change and increased composite thermal conductivity as discussed above, but not by softening the composite (as it is unlikely to impact R'_{int} because skin is the softer of the two materials). Specifically, the model indicates that at low contact pressure R'_{tot} is about 2.6 m°CW^{-1} for pure rectangular silicone tubes and could be reduced to 1.5 m°CW^{-1} and 1.2 m°CW^{-1} by increasing ϕ to 0.3 to 0.5, respectively (see Figure 2.5). The plots of the segregated

sub-models in Figure 2.5 reveal that R'_{int} is the predominant contributor to R'_{tot} . This plot also demonstrates that R'_{int} can be substantially decreased by 0.4 to 0.6 m°CW^{-1} by simply applying higher contact pressure (6 kPa), resulting in a significantly lower R'_{tot} of 1.9, 1.1, and 0.8 m°CW^{-1} at ϕ of 0, 0.3, and 0.5, respectively. Since this value of pressure is near the lower threshold for discomfort found by Denton (5.88 – 9.80 kPa),[79] increasing the contact pressure beyond this value is not recommended from comfort perspective. In addition, further increase is unlikely to provide any cooling capability improvements because skin contact resistance saturates rapidly after few kilopascals of pressure is applied[69] (i.e. thermal gains are likely even with lower applied pressure in the range of 3 to 4 kPa, which is in the pressure comfort zone). As such, the necessary increase in contact pressure could be easily achieved by integrating the composite tubing under elastic, tight fitting clothing (e.g. spandex) or simple tightening of the compliant tube around the body. To further lower the interfacial resistance, a thin layer of a biocompatible thermal interface material such as a sweat-capturing hydrogel could also be included. Even without such interface engineering, the predicted total resistances are significantly lower than those of current thermoregulatory LCJs made of PVC, which for our control device I measure to be at least on the order of 3 to 4 m°CW^{-1}. Thus, these results indicate that contour alteration and materials engineering could substantially decrease the thermal resistance of tubes. Naturally, systematic human-testing, which is beyond the scope of our current work, should be conducted to provide definitive verification of this notion.

2.2.5 Impact of Low Resistance Tubing on Overall Cooling System

Lastly, I evaluate the enhancements in cooling capability as well as the reduction in the device's size/weight that could be attained through total thermal resistance reduction via geometry and material augmentation. In order to use Equation 2.1 to calculate the total rate at which the simulated LCJ removes heat, $\dot{Q}$, we need to first estimate the $T_{m,out}$ for a given tube length:[71]

$$T_{m,out} = T_s - (T_s - T_{m,in})\left(e^{-\frac{1}{\dot{m}c_p R_{tot}}}\right) \tag{2.13}$$

Substituting Equation 2.13 into Equation 2.1, we obtain:

$$\dot{Q} = \dot{m}c_p(T_{m,out} - T_{m,in}) = \dot{m}c_p(T_s - T_{m,in})\left(1 - e^{-\frac{1}{\dot{m}c_p R_{tot}}}\right) \tag{2.14}$$

Where $R_{tot} = R'_{tot}/L_{tube}$ is the total thermal resistance of the device.

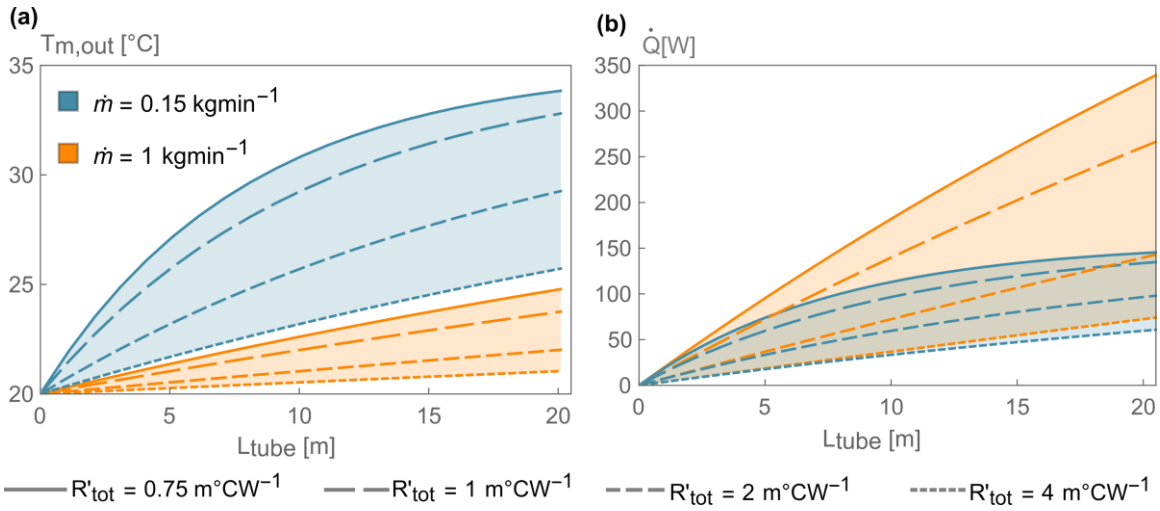

Figure 2.6 Plots of a) mean outlet water temperature ($T_{m,out}$) and b) total heat removed ($\dot{Q}$) as a function of the tubes' length (L_{tube}) for various R'_{tot} and low (laminar indicated with light blue shade) and high (turbulent indicated with light orange shade) mass flow rates, simulated at a $T_{m,in} = 20\ °C$ and $T_s = 35\ °C$.

The plots in Figure 2.6a-b show the $T_{m,out}$ and the $\dot{Q}$ for tubing length up to 20 m (typical for an upper body vest) for devices with R'_{tot} of 0.75 m°CW^{-1} (composite device with $\phi = 0.3$ with interfacial layer and good contact), 1 m°CW^{-1} (composite device with $\phi = 0.3$ with good contact), 2 m°CW^{-1} (composite device with $\phi = 0$ with good contact), and 4 m°CW^{-1} (PVC device with poor contact). The plots also include predictions for laminar flow (0.15 kg min^{-1} used in this work) and turbulent flow (1 kg min^{-1} typically used in full body liquid-cooled garments). These plots reveal that for the high thermal resistance PVC device with 20 m of tubing, the total removed heat is nearly identical (60 to 70 W) for both mass flow rates. When the tube's resistance is lowered, its length required to remove the same amount of heat decreases drastically. In particular, when R'_{tot} is lowered to 2 m°CW^{-1}, 1 m°CW^{-1}, and 0.75 m°CW^{-1} only 12 m (60% of 20 m), 6 m (30%), and 4.8 m (24%) of tubing is required to remove 70 W with laminar flow. For the same reductions in total resistance, applying turbulent flow results in a further reduction in tubing length with only 9.5 m (48%), 4.8 m (24%), and 3.5 m (18%) being required to remove 70 W. However, if we consider the drastic increase in pressure drop and thus required pumping power affiliated with turbulent flow (see plot in Figure 2.7), using a low resistance device that operate in laminar flow regime is optimal for short LCJs. Furthermore, note that for the lowest resistance tubing with length below 5 m, the heat extracted in both flow regimes is almost equal, thus extra pumping power required for transition to turbulent flow is wasted on applications requiring short tubing length (e.g. very compact LCJs). That being said, for low resistance devices operating in laminar regime with more than 12 m of tubing, the coolant temperature starts approaching that of

the substrate (i.e. thermal stagnation can be reached), producing unevenly distributed heat extraction. Thus, use of low resistance tubing operating in laminar regime only makes sense for applications requiring a minimal length of tubing.

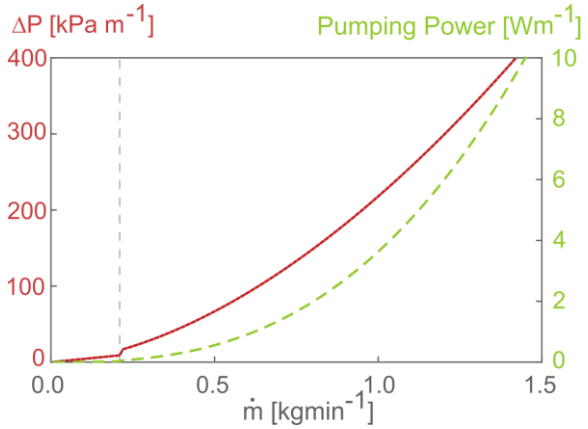

Figure 2.7 Calculated pressure loss (ΔP) per meter and pumping power per meter of the tubing as a function of the mass flow rate, the vertical dashed line indicates the flow rate at which the flow regime transitions from laminar to turbulent.

Intriguingly, this disparity in heat extracted between flow regimes presents the opportunity of operating the cooling devices at a low flow rate ("economic setting") with moderate heat removal and low power requirement as well as at a high flow rate ("sport setting") with high heat removal capability and moderate power requirement. For example, the heat transfer rate removed by a 12 m long tube with R'_{tot} of 0.75 m°CW^{-1} could be increased by almost 100 W by switching these modes. If much higher heat removal rates are desired, the low resistance tubes should operate at turbulent flow with increased length. For example, the plots in Figure A9 show that LJCs consisting of 20 m, 60 m, and 100 m of the low resistance tubing with mass flow rate of 1 to 1.5 kg min^{-1} could remove 250 to 350 W, 600 to 900W, and 800 W to 1150 W, respectively. In contrast, the model shows that high resistance devices with 100 m of PVC tubing can

remove only around 300 W, which is in good agreement with reported capabilities of current LCJs.[33]

Finally, comparing the weight of the 5 m long cooling tubes, the round PVC control was much lighter (64 g) than the composites devices (187 – 234 g for ϕ = 0 – 0.3). This increase stems from switching from round to rectangular geometry and the addition of Al filler particles (weight increase by 25 % for ϕ = 0 – 0.3). However, this weight gain can be offset by the reduction in necessary length of tubing (up to 75% less) for a given cooling need. For example, a 20 m PVC tube weights about 250 g, which is higher than a 5 m silicone tube with ϕ = 0.3. Additionally, a major latent reduction in system weight would be achieved here, since the required battery capacity for the pump would also reduce proportionally to the length of tubing (or could remain constant allowing for longer periods of operation).

2.3 Summary

In Chapter 2, I explore the effects of transitioning to a soft, surface deformable SHX under steady state static conditions in the setting of a liquid cooling device for thermoregulatory, electronics, and robotics applications. To do so, I build an experimental hot-plate test setup and evaluate the thermal performance of prototype liquid-cooled SHXs made of Silicone-Aluminum composites of varying filler fractions. Using a combination of sub models, I build and validate a closed form, steady state, thermomechanical model that predicts thermal performance as a function of tube geometry and filler fraction. The model is then used to explore a variety of avenues to optimize SHX design to minimize the required length of tubing while maximizing the

heat extracted. The potential benefits of each methodology are summarized relative to a control device made of PVC and of note, much of the thermal performance increase was brought about by a geometric shift from a circular to rectangular cross section. Additionally, I speculate the viability of the model in a variety of other scenarios, such as SHXs in contact with skin as opposed to a metal surface. Finally, I illustrate the necessity of a holistic design approach, that takes into account total thermal resistance of a tubing network, flow regimes, temperature distributions and pumping power to achieve optimal performance for a given application.

CHAPTER 3

3. SOFT HEAT EXCHANGERS UNDERGOING LARGE DEFORMATION DURING OPERATION

Though the previous chapter highlights a model to predict performance under steady state conditions, SHXs are unlikely to be static in their final operating conditions and instead would be subjected to stretching. Dynamic shape change either intermitently or periodically could drastically deviate thermal performance from static, steady state predictive models. Thus, there is a need to understand and quantify the effects of in-operation shape deformation on the thermal performance of SHXs. However, such a task is not a trivial undertaking since transient device shape change invalidates many conventional assumptions employed in heat exchanger design[2,71] including a static diameter, length, and wall thickness as well as constant flow, material properties, and boundary conditions. To begin exploring the novel concept of a soft, stretchable heat exchanger undergoing large shape change during operation, I fabricated elementary single-stream, water-cooled devices out of silicone with 0% and 20% volume fraction of liquid metal micro-droplets averaging a diameter of 60 μm (see Figure 3.1a-c and Figure B1 for further details). As illustrated in Figure 3.1c, stretching the tube expands the inner diameter and elongates the LM micro-droplets, resulting in anisotropic thermal properties that need to be considered. The tubes are embedded with steel extension springs to serve both as an extensible joule heater and a resistive temperature probe (see Figure 3.1a-b). These heated tubes are incorporated as a stretchable section of a carefully designed and

calibrated flow loop. I used a linear actuator to continuously stretch and retract the heated soft tube from an initial 15% to a 45% stretch at a constant rate ranging from 0.3 to 8 mms^{-1}. I discuss further details in the Experimental section.

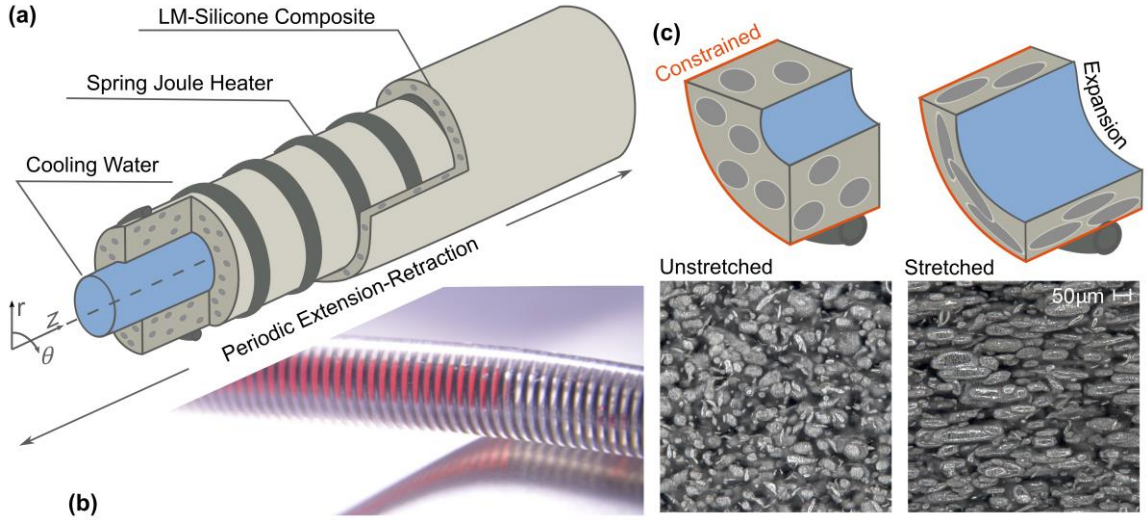

Figure 3.1 Illustration (a) and photograph (b) of an example single-stream soft heat exchanger; in (b) only silicone was used to make the tube to make the extension spring embedded in the tube wall as well as dyed red water in the inner cavity visible; (c) top row schematically shows the eff of axial extension on the tube wall, inner channel, and the liquid metal micro-droplets; the bottom row shows the microscopic view of the effects of tube stretching on the liquid metal droplets.

Using a time scale analysis, I identify conditions under which the quasi-static assumption is applicable. In this gradual shape modulation regime traditional fixed-geometry and material property models can be extrapolated to consecutive time steps to predict the devices thermal performance. I validate our time scale analysis by experimentally characterizing thermo-fluidic performance of our soft heat exchanger as it undergoes axial stretching and retraction during operation.

3.1 Experimental Methods

3.1.1 Soft heat exchanger fabrication

The composites were fabricated by dispersing the filler particles in a two-component silicone (SmoothOn, SortaClear 14 A and B). In this study, I used a liquid metal filler particles which were fabricated by high-speed shear mixing liquid metal eutectic GaInSn, prepared in house (Ga 68%, In 22%, Sn 10%, all obtained from RotoMetals), in an ethanol solution until the desired particle distribution with an average of about 60 μm was achieved (see Appendix B for details). Once the appropriate particle distribution was achieved, I removed as much of the ethanol from the top as possible with the use of a syringe while maintaining enough to ensure the liquid metal suspension did not recoalesce. I then mixed the filler particles into the silicone component A with the use of a high-speed mixer (Dremel 3000) to ensure even dispersions and then further mixed with the silicone component B. The final mixture was then degassed in a vacuum chamber to remove air that was incorporated in the mixing process and any remaining ethanol. Finally, the mixtures were injection cast at a rate of 0.5 $mlmin^{-1}$ into molds consisting of vertically hung glass tubes (McMaster # 8729K33, 5.59 mm inner diameter) with a centered nylon line (Catch All Tackle sku:2519933, 1.9 mm dimeter under tension) kept under a constant tension along the tube axis, and an extension spring (McMaster # 9664K74, 3.96 mm inner diameter) stretched to 275 mm (see Appendix B for further details). The pre-extension of the spring allowed for the composite mixture to flow into the gaps between the coils and ensured that there was no electrical short between neighboring spring coils. Due to difference between the glass tube inner

diameter and the spring outer diameter and its pre-extension, a layer of the silicone mixture forms around the coil, effectively embedding a stretchable joule heater in the tube wall. The final mold was then hung under a constant tension and allowed to cure for 16 hours at lab temperatures 18 to 20°C. Post cure, with the use of isopropanol alcohol I extract the prototypes and formed electrical leads at both ends of the device by exposing and unravelling parts of the spring coil. I note that I also fabricated tubes with composites with higher content of LM (30-50%), however, I found that these materials were leaking liquid metal as well as water through pinholes during operation.

3.1.2 Thermal Characterization

The thermal conductivity of the materials were measured using a Hot Disk Thermal Constants Analyzer (Thermtest,TPS2500S). To satisfy the infinite sample assumption underlying this method, it is recommended that the thermal wave probing depth be smaller than the smallest sample dimension, calculated as $\Delta_p = 2\sqrt{\alpha t}$, where α is thermal diffusivity of the sample and t is the run time of the experiment. Based on previous experiments, it was estimated that for these materials the maximum $\Delta p \approx 6$ mm.[9] Consequently, 10 mm thick disks with 25 mm diameter were cast. Three sets of samples for the silicone and 20% liquid metal composite were fabricated and tested. The measurements using sensor design 5465 (3.2 mm radius Kapton sensor) were carried out, with a measuring time of 20 s and a heat flux of 50 and 80 mW for the silicone and composite, respectively. In this test method, the heat sensor was used as both a heat source and a temperature sensor and thus measured both the heat input, output, and the temperature increase in the sensor. Using this transient data, the hot disk iteratively

calculated the thermal conductivity and thermal diffusivity values with a manufacturer specified accuracy of ±5%.

3.1.3 Testing Procedure

To explore the thermal performance of the stretchable devices, I developed the flow loop illustrated in Figure 3.2a. I set the inlet temperature to 10°C to ensure minimal thermal degradation and thermal expansion of the composite, the importance of which is discussed later, by using a temperature-controlled circulating water bath (45 L version

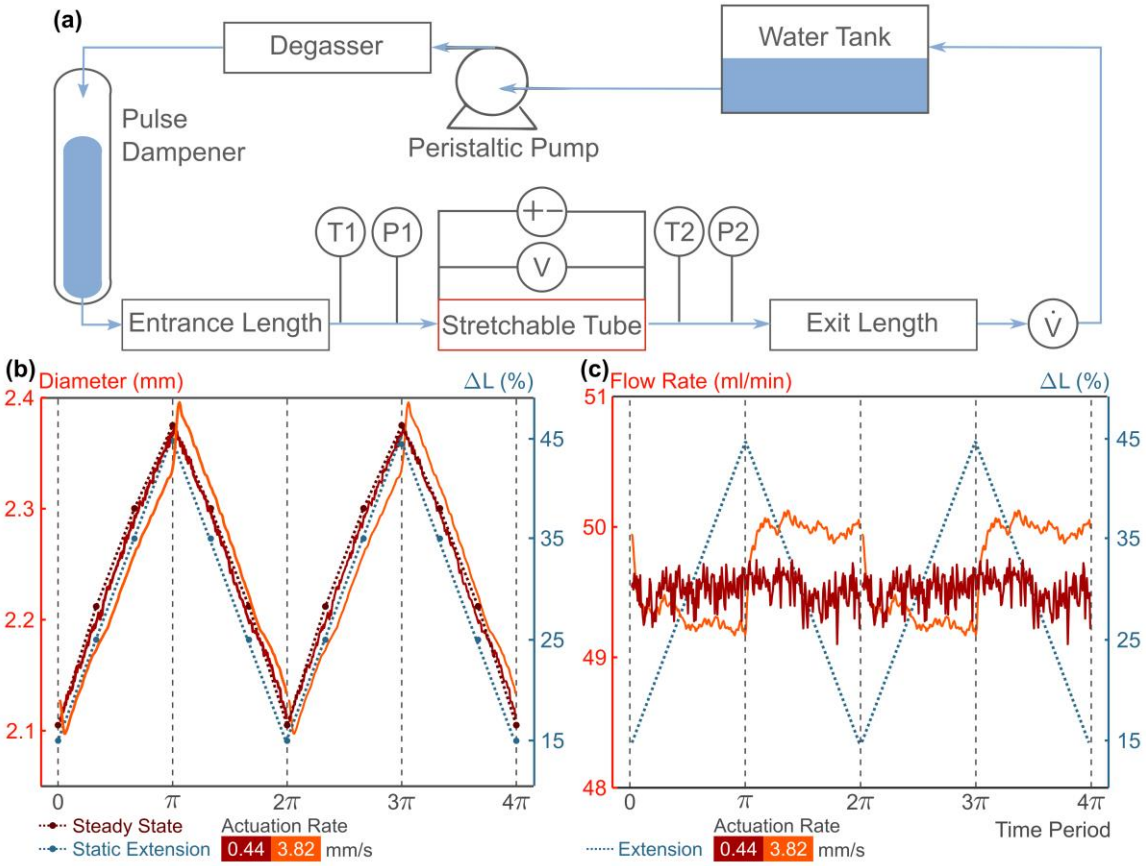

Figure 3.2 (a) An illustration of the flow loop that was implemented in this study, (b) the effect of stretch-retraction of the tube on its inner diameter with a static extension, a slow actuation rate of 0.44 mms^{-1}, and a fast actuation rate of 3.82 mms^{-1}, and (c) the effect of stretch-retraction on the flow rate through the device.

from VWR). The cooling water was pumped at a constant flow with the use of a peristaltic pump (OMEGA FPU500) and, in order to ensure a constant laminar flow into the stretchable device, the flow was fed into a custom-built pulse dampener. Prior to entering the test section, the flow was fully developed hydrodynamically with the use of an entrance length of the same inner diameter as the devices, D =1.9 mm, and a length of 300 mm which is well above the recommended length of $50D$ the inner diameter obtained from the $0.05ReD$ expression (Re corresponds to the Reynolds number).[71] To prevent any hydrodynamic exit effects, an exit length identical to the entrance length was fitted after the test section. The flow from the device was monitored and recorded with the use of an inline flow sensor (OMEGA FLR1007) after the exit length, from where the cooling water was recirculated back to the water bath. The test section itself was fitted with a prototype device which was heated by running a constant current of 1.9A through the spring coil. The device, during operation, was linearly and periodically stretched in a tensile fashion from an initial 15% stretch, that was chosen to avoid any tube sagging, to up to 45% over the original tube length at multiple rates, ranging from 0.3 - 8 mm/s, with the use of linear actuators (Firgelli Feedback Rod Linear Actuators with 20 cm extension and 200 lbs capability, see Appendix B for further information). Finally, the test sections external environment was controlled with use of flexible insulation in the form of cotton frills that were hung from the containment ceiling. The frills were used to ensure a high, constant thermal resistance to the environment, independent of stretch rate.

The testing procedure consisted of allowing the flow to reach a steady state of 50 $mlmin^{-1}$, and then heating the device via the joule heater. Once the ambient temperature

measured directly above the tube did not vary more than +/- 0.5°C over 10 minutes, steady-state was achieved and the device was actuated. For each stretch rate, a 10 minute initiation period was followed by 20 minutes of data collection. In between individual stretch experiments, at least a 2 minute unperturbed period in which flow achieved steady state was introduced. During testing the pressure drop (OMEGA PX2300-1DI), temperature difference (PTC10 with T-type thermocouples), the voltage across the test device, the length/extension (via the in-built potentiometer in the actuator), and flow rate were measured at a frequency of 4 Hz. For each tube composition and extension rate, experiments were repeated four times. In addition, I conducted control experiments with fixed tube extension of 15, 25, 35, and 45%.

3.1.4 Experimental Considerations and Raw Data Analysis

By nature of this system, I observed a coupling of mechanical, thermal, and fluid properties, which I outline individually below. Concerning the mechanics of deformation, the tube mechanics are dominated by the steel spring embedded in the device wall. Due to the pseudo outer-wall constraint imposed by this spring, when extended the tube inner diameter expands instead of contracting. From experimental characterization, I found this behavior to be in between a tube that is mechanically unconstrained and fully constrained at its outer-wall (see Appendix B for further discussion). To overcome this complex nature of tube deformation and to account for other effects induced by rate of stretching or thermal changes, I back-calculated the inner diameter of the tube from the measured pressure drop using the Hagen-Poiseuille law for pressure drop across a pipe with laminar flow:[71]

$$\Delta P = -\frac{128\mu\dot{V}L}{\pi D^4} \quad (3.1)$$

Where, ΔP is the pressure drop across the test section, μ is the viscosity of water at a mean fluid temperature between the inlet and outlet, $\dot{V}$ is the flow rate, and L is the length of the test section. By measuring each of these variables during actuation, I calculate the inner diameter of the tube also during actuation, as illustrated in Figure 3.2b. Since the steel extension spring does not constrict during extension, I am also able to calculate the wall thickness between the spring (constant inner diameter of 4 mm) and the tube inner wall, which is the characteristic conduction heat transfer length used to calculate t_k, the characteristic conductive time scale. I observed that diameter deformation is most drastic in the first 15% of extension, after which rate of change with extension slows down. As noted previously, to avoid any sagging effects, our extension ranged from 15% to 45% of the original length. Finally, I note a weak coupled effect between the wall temperature and the tube mechanics stemming from thermal expansion of the material. In my exploratory experiments, I ran 2A of current through the test devices and observed spring temperatures of up to 120°C and a deviation of diameter by up to 6% of the expected value. To mitigate these effects, I reduced the spring temperature by reducing the current to 1.9A and by running colder water maintained at 10°C at the inlet.

With regards to the hydrodynamics, in order to ensure accurate predictions through the Hagen-Poiseuille law, I maintained laminar flow by ensuring a Re below 500 for all tube extension states. I achieved this with the use of a small inner diameter combined with a low inlet temperature (10°C), to increase viscosity, and a low flow rate (50 $mlmin^{-1}$). Furthermore, in the work by Kumaran et al[80–82], a hydro-mechanical relation between

the shear modulus of the tube and turbulence transition Re number was highlighted (i.e. softer tubes promote transition to turbulence). Kumaran also quantified the extent of tube inflation, by drawing a correlation between material softness and the Re number. By using a silicone matrix with a shear modulus of ~50 kPa and $Re < 500$, we stayed below the lowest transition point of $Re \approx 500$ (reported for a soft gel-silicone with a shear modulus of ~18kPa), and ensured negligible tube inflation due to flow.[82] Thus, with these considerations, I ensured minimal effects of fluid dynamics on the system. In other words, the cooling fluid acted as a thermal sink for the heat generated by the spring and provided means of quantifying the inner diameter during operation.

Finally, though I isolated the tube mechanics from the hydrodynamics, I note that there is a coupled effect of the tube mechanics on the fluid flow in the form of a pumping effect caused by periodic expansion-contraction that creates flow fluctuations proportional to the rate of actuation. This effect can be clearly seen in Figure 3.2c where, at an actuation rate of 4 mms^{-1}, the flow takes on a square wave profile. In our exploratory experiments, we found this profile eventually becomes sinusoidal in nature if the rate is increased further. However, these flow oscillations induced by the tube actuation only occur at higher actuation rates and are below 5 $mlmin^{-1}$ (i.e. 10% of used flow rate) in the range of actuation rates that I report data for, thus can be neglected.

To quantify the thermal performance of the devices, I evaluated the spatially averaged spring temperature. To do so, I measured the electrical resistance of the spring coils, embedded in silicone, as a function of temperature in a combination of water and silicone oil baths to achieve a wide range of temperature calibrations points. By doing so, I

evaluated the temperature coefficient (γ) of our spring to be 0.0272 Ω/°C, which matches other previously reported values for steel[83] (see Appendix B for further information). Finally, a reference temperature, T_{ref}, of about 73 °C was chosen to minimize the deviation that the linearization of the temperature resistance curve could cause. The resistance of each tube at a simillar temperature was measured by submerging the tube in a homogenous, constant temperaure water bath and used as the reference resistance, R_{ref}. To calculate average spring temperature, T_s, from the measured spring resistance, R_{spring}, at other conditions I used the following equation:

$$T_s = T_{ref} + \frac{R_{ref} - R_{spring}}{\gamma} \tag{3.2}$$

In a silicone tube we estimated the spring temperatures to oscilate about ~95°C, while with a liquid metal silicone composite, oscilations were about ~55°C for the same operating conditions. This demonstrates the expected increase in thermal performance (about a 60% increase) in transitioning to these more thermally conductive composites.

I ensured that the majority of generated joule heating within coil ($\dot{Q}_{supply} = VI$) was removed by the cooling water by comparing it with the heat removed by the water. I calculated the total heat transfer rate to the cooling water, $\dot{Q}_{in}$, using the following equation:[71]

$$\dot{Q}_{in} = \dot{m} c_p \left(T_{m,out} - T_{m,in}\right) \tag{3.3}$$

Where $\dot{m}$ is the flow rate, which is set to 0.8 gs^{-1} (50 $mlmin^{-1}$), $T_{m,in}$ and $T_{m,out}$ are the mean inlet and outlet water temperatures, and c_p is the specific heat taken as 4184 J/kg°C. The current supply was kept constant (1.9A) and the voltage across the device

was actively collected. By comparing the $\dot{Q}_{supply}$ to $\dot{Q}_{in}$, I evaluated the effectiveness of insulation and it was found to minimize heat loss to air down to 10% of the $\dot{Q}_{supply}$ (see Appendix B for further details).

3.2 Results and Discussion

The used geometrical and operational settings allowed us to vary time scales over the range required to validate our analysis and discuss applicability of and deviation from predictions based on the quasi-static shape assumption. By doing so, I set up a guideline on how such transient problems can be approached and how to evaluate the complexity of a soft heat exchanger system. Next I discuss the details of the time-scale analysis and experimental characterization of the thermal performance of the device used to validate our theoretical notions.

3.2.1 Time-scale analysis of the soft heat exchanger operation

Predictive models based on the quasi-static assumption are often employed to overcome the complications of transient models. These models assume that the time scales of transient effects occur rapidly enough to consider the changes as discrete incremental states that achieve a steady state prior to transitioning to the next state, i.e quasi-static. In order to evaluate the validity and applicability of the quasi-static assumption to a system, we must identify and compare relevant characteristic time scales for the occurring physical processes. For a soft heat exchanger, primary modes of heat transfer are conduction across the tube wall and internal forced convection from the tube wall to the water. The characteristic time for convection (t_c) can be thought of as the average time taken by a water molecule moving with mean axial velocity ($U \approx$237 to 190

mms^{-1}) to travel through the tube length (i.e. $t_c = L/U$). In turn, the characteristic time scale for the conduction of heat across the wall with thickness $h \approx 1$ mm that is composed of material with transverse thermal diffusivity ($\alpha \approx 0.13 – 0.34$ mm^{2}s^{-1}) is equal to $t_k = h^2/\alpha$.[84] Substituting our experimental system's values, we find that t_c ranging between 1 to 2 s is smaller than t_k, which ranges between 4 to 7 s. In other words, in response to a perturbation in the tube shape a near steady-state temperature profile will be established within the liquid significantly quicker than in the tube wall. Consequently, I simplify our problem formulation by setting t_k as the characteristic thermal time scale.

The characteristic thermal time scale must be compared against the device deformation time scale (t_d) which, due to the periodic oscillations of the system, I set to one tube stretching-retraction period (i.e. one wave period). If the tube is stretched to ΔL (maximum of 64 mm) and the tube is actuated at rate L', $t_d = 2\Delta L/L'$. In terms of the actuation angular frequency, ω, $t_d = 2\pi/\omega$. By adjusting the device actuation rate, I can vary t_d between 16 s and 300 s and explore regimes where $t_k/t_d \approx 1$ and $1 \gg t_k/t_d$. While our equipment limitations did not allow us to study the $t_k/t_d \gg 1$ regime, I will show later that it is not necessary in determining the limits of t_k/t_d where the quasi-static shape assumption is valid.

3.2.2 Thermofluidic characterization of soft heat exchanger operation

To evaluate the cooling performance of the soft heat exchanger I embedded a steel extension spring near the outer wall of the tube wall to act as both a joule heater and a resistive temperature probe. Specifically, by maintaining a constant 1.9A current through

the spring while allowing the voltage to vary, during actuation I can measure both the heat generated ($\dot{Q}_{supply} = VI$) and the fluctuations in electrical resistance that are due to resistivity changes with temperature ($R = V/I$). Using the proportional relationship between electrical resistance and temperature (temperature coefficient for spring steel of 27 $m\Omega/$°C), I can calculate the spatially-averaged spring (heater) temperature (T_s). Out of the numerous variables that I measured, I found T_s provides the most representative and sensitive metric to quantify cooling changes associated with stretching the tube. In qualitative terms, the heater temperature will be proportional to the thermal resistance between the heater and cooling water. Specfically, the point at which T_s is lowest will represent the point at which the thermal resistance posed by the wall and convection is lowest or, in other words, when the heater is most effectively cooled.

In Figure 3.3 I present T_s results for tubes made out of only silicone (Figure 3.3a) and a 20% LM-silicone composite (Figure 3.3b). To facilitate one-to-one comparison between the two materials, I plot the demeaned spring temperature, i.e $\Delta T_s = T_s - \bar{T}_s$. Additionally, to clarify comparisons across the various stretch rates, the collected thermal data from each stretch rate was cyclically averaged across all studied oscillations and compiled into a single stretch-retraction cycle, converting time series data to periodic data (0 to 2π radians). Finally, for clear representation of the oscillatory nature of the system, this averaged stretch-retraction cycle is simply repeated so that the plots in Figure 3.3 range from 0 to 4π radians.

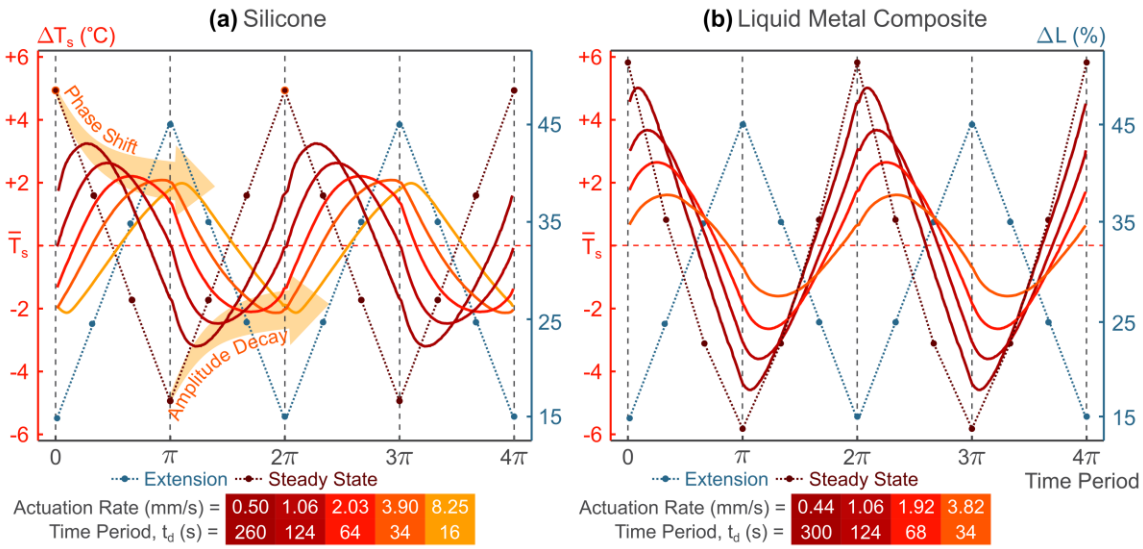

Figure 3.3 Representative demeaned spring temperature over two cycles of extension-retraction for (a) a silicone tube with highlighting arrows to show the rate dependent phase shift and amplitude decay and (b) for a liquid metal composite tube consisting of 20% liquid metal volume fraction.

To set the baseline quasi-static predictions, I conducted steady state control experiments with fixed extensions (i.e. $t_d \to \infty$). As shown in Figure 3.3, I studied steady-state behavior in tubes that were extended to 15%, 25%, 35% and 45 % above the original length of about 254 mm (blue dots connected by dotted line that form a triangular wave). In our generalized representation, the corresponding ΔT_s that were measured during the non-actuated but stretched tube experiments also form a triangular wave that corresponds to ideal quasi-static behavior, indicated by the brown points connected by dashed lines in Figure 3.3. Since at maximum extension (45%), the wall thickness is at its minimum (0.82 mm) and the convective heat transfer surface area is at its maximum (23.7 cm^2), the wall-cooling rate is at its maximum translating into lowest ΔT_s of -4.9°C for the silicone tube and -5.8°C for the composite tube. This value is 10°C to 12°C lower than ΔT_s measured for the lowest tube extension (15%), for which tube

thickness is a its maximum (0.94 mm) and the convective heat transfer surface area is at its minimum (16.9 cm^2).

When the tubes are actuated during operation, the ΔT_s deviates from the ideal quasi-static triangular wave in two ways. First, the amplitude of the oscillations decreases with increasing actuation rate. For example, for a silicone tube the static 15% extension results in a ΔT_s max of 4.9 °C but with actuation rates of 0.5 and 3.9 mms^{-1} the maximum ΔT_s drops to 3.2 °C (-35%) and 2.1°C (-57%), respectively (see Figure 3.3a). For the composite tube the static 15% extension results in a ΔT_s of 5.8 °C but with actuation rates of 0.44 and 3.82 mms^{-1} the maximum ΔT_s drops to 4.4°C (-24%) and 1.5 °C (-74%), respectively. Second, it is evident from Figure 3.3 that the deformation of the tube introduces a phase lag in ΔT_s that is proportional to the actuation rate. I discuss this phase shift (φ) in terms of π (radians) deviation from the quasi-static triangular wave. For example, for the silicone tube with actuation rates of 0.5 and 3.9 mms^{-1} I measure a φ of 0.26π and 0.91π, respectively (see Figure 3.3a). For the composite tube with actuation rates of 0.44 mms^{-1} and 3.82 mms^{-1} there is a smaller φ of 0.09π and 0.34π, respectively. Consequently, our data shows that in all cases I have studied the thermal performance of the actuated soft heat exchanger departs from the static extension values. In other words, a quasi-static assumption based analysis would not be valid for the actuation rates that I was able to experimentally study with our setup. Next, I show that by re-evaluating the ΔT_s in terms of the previously discussed time scale ratio and considering a classical analytical model for an oscillating boundary condition problem,[85] I can generally predict how slow actuation would have to be for the quasi-static assumption to be valid.

3.2.3 The characteristic time scale ratio and shape-modulation regimes

Figure 3.4a shows that the ΔT_s phase-shift data for silicone and composite tube actuation experiments both clearly decay with increasing device time scale (t_d). Furthermore, when presented as a function of the previously introduced conduction to device time scale ratio (t_k/t_d), the two data sets collapse into a single general curve that elucidates the role of the relative magnitudes of the characteristic time scales (Figure 3.4b). Specifically, our experiments cover φ data for t_k/t_d of about 0.6 down to 0.006. In the $t_k/t_d \approx 1$ regime, the over 1π phase shift results in a complete inversion of ΔT_s from the representative quasi-static behavior (i.e. T_s is heating up rather than cooling down when the tube is extending). As the t_k/t_d ratio decreases to 0.1, the phase-shift also decreases substantially to 0.25π. However, as the t_k/t_d ratio decreases even further the rate of φ decay decreases. With our most extreme measurement of t_k/t_d of 0.006 that corresponds to the slowest actuation (0.44 mms^{-1}) of the LM composite tube, the phase-

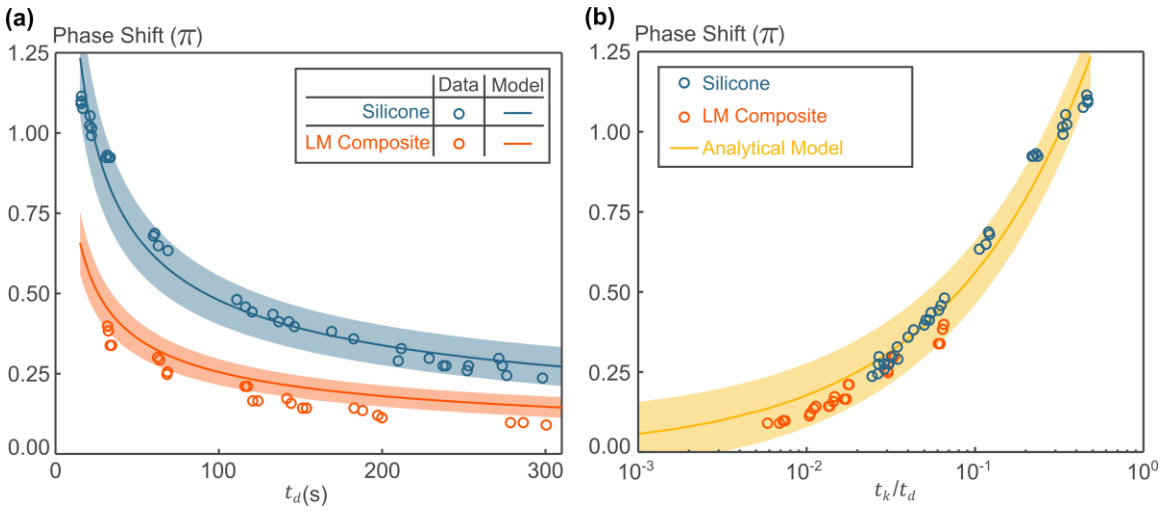

Figure 3.4 The measured and theoretically predicted spring temperature phase shift as a function of (a) the device actuation time scale, t_d and (b) the dimensionless ratio of the conductive to device actuation time scale, t_k/t_d

shift decreases to 0.09π, representing a 9% temporal deviation. It is also evident from Figure 3.4b that this combination presents the closest actuated ΔT_s curve to the representative curve of the quasi-static assumption. Thus, while close, the experimental data still does not reach a regime in which the quasi-static assumption would be representative of the system behavior (defined here as a temporal deviation smaller than 2%). However, using a simple model that relates the time scales to the phase-shift which match the data, I show that conditions under which this assumption is valid can be estimated.

The thermal system can be thought of as a wall undergoing periodic temperature change at its boundary, so it belongs to the general class of heat transfer problems with periodic boundary conditions. Thus, we can gain insight into the transient heat transfer processes occurring in soft heat exchanger operation by exploring the functional forms of solutions to such periodic problems. For example, the analytical solution for the temperature profile ($T(x,t)$) of a semi-infinite medium, undergoing periodic temperature fluctuations at the wall boundary is:[85]

$$T(x,t) = Aexp(-Kx)\cos(\omega t - Kx) \tag{3.4}$$

Where, A is the amplitude of the periodic temperature oscillations, x is the depth into the semi-infinite medium from the thermally oscillatory surface, ω is the angular frequency of surface thermal oscillations, and K (m^{-1}) is the wave number that is defined as $(\omega/2\alpha)^{1/2}$. While this model neglects the finite nature and the shape modulation aspect of our system, the functional form agrees with two key trends in our experimental data, namely, the phase shift and amplitude decay that is proportional to frequency of

oscillation. By manipulating the previously introduced definitions of the time scales I obtain $\omega = 2\pi/t_d$ and $\alpha = x^2/t_k$. By substituting these relations and employing the wall thickness for the characteristic length (i.e. $x = h$), I obtain an expression for the phase-shift ($\varphi = Kx$) in terms of the characteristic time scale ratio, t_k/t_d:

$$\varphi = Kx = Kh = \left(\pi \frac{t_k}{t_d}\right)^{1/2} \tag{3.5}$$

As shown in Figure 3.4b, when the variation in h and α is taken into account (see discussion below), this simple model provides an excellent prediction of the measured phase shift data. In other words we can, with confidence, use this simple relationship to extrapolate the data and determine the value of φ at $t_k/t_d < 0.006$. For example, for t_k/t_d of 10^{-3} we can expect a very small φ of 0.015π that can be considered negligible (below 2% of the time-period). If we also take into account that the difference between ΔT_s maximums for the quasi-static curve and the actuated curves decreases with φ (see Figure 3.5), using linear extrapolation we can estimate that t_k/t_d of 10^{-3} the ΔT_s will be within 0.25°C of static values. Consequently, I assert that t_k/t_d of 10^{-3} sets an appropriate threshold for the gradual shape modulation regime ($t_k/t_d \ll 1$), where models based on the quasi-static shape assumptions are appropriate for soft heat exchanger design. If t_k/t_d is greater than this value, the device will operate in a 'rapid' shape modulation regime where transient shape effects must be taken into account for accurate system modeling.

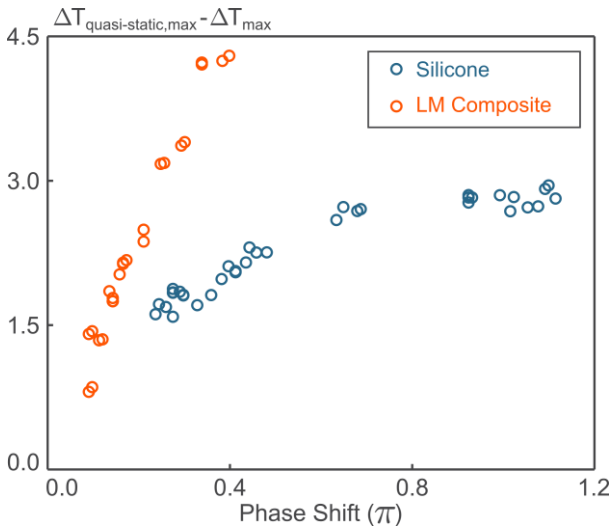

Figure 3.5 The difference between peak average spring temperature in nonactuated (quasi-static like) and actuated conditions as a function of the corresponding phase-shift.

While equipment limitations did not allow me to experimentally probe the regime of $t_k/t_d \gg 1$, the increasing phase shift and decreasing amplitude trends observed in Figure 3.3 and 3.4 suggest that eventually the magnitude of oscillation might saturate and, for more thermally conductive tubes, even flatten out (i.e. the concept of a phase shift would no longer be applicable). However, in this very rapid shape modulation regime other phenomena are likely to have a more significant impact on the soft heat exchanger performance because the device actuation time scales will become comparable or smaller than the convective and hydrodynamic time scales (≈1 s). The behavior of soft heat exchangers in this regime presents an interesting area for future exploration and could warrant an analysis encapsulating three or more time scales.

Lastly, I discuss the impact of LM micro-droplet shape transition brought about by tube extension, that is evident in images in Figure 3.1c, which imparts anisotropy to the composite thermal properties. This temporal micro-structure change will introduce

associated temporal variations in α and, in turn, t_k. While the directionality of α in LM composites under strain has not been explicitly studied, it is likely to be proportional to the changes in thermal conductivity since diffusivity is defined as $\alpha = k/\rho c$ (where density ρ and specific heat c are compositional values and should not be impacted by mechanical deformation). Bartlett et al.[1] demonstrated that along the direction of stretch in a rectangular slab, thermal conductivity increases by up to five fold. For heat transfer from the spring to the cooling water, it is the transverse thermal conductivity that is relevant (in the plane normal to the axis of the streched LM droplets in Figure 3.1c). This value, $k_{transverse}$, is commonly evaluated from the geometric mean of the conductivity in the associated two axes, which if you consider this problem from an axisymetryic perspective, the transverse plane will consist of the radial (r) and axial (z) axes and so, $k_{transverse} = \sqrt{k_r k_z}$.[1] Using approximated values from Bartlett et al.,[1] I estimate that with the 45% extension of the LM composite tube the transverse α will increase from 0.34 mm^2s^{-1} that was measured at 0% extension to 0.46 mm^2s^{-1} (vs. 0.13 mm^2s^{-1} for the silicone matrix). In fact, I speculate that the α increase could potentially be even higher due to the particle deformation in the θ direction as well (see Figure 3.1c). While thorough validation of these values is beyond the scope of the current work, the fact that in Figure 3.4 most experimental data is captured by the model envelope for which I used a α of 0.46 mm^2s^{-1} for t_k and the potential for the remaining deviation to be met by a further increase in diffusivity, suggest merit to my analysis.

3.3 Summary

In Chapter 3, I explore the effects of transient shape deformation during SHX operation and outline a fundamental approach to designing such systems. To do so, I build a carefully calibrated flow loop along with prototype single-stream liquid cooled SHXs with Galinstan-Silicone composites to experimentally explore this concept. I found that when the SHXs were axially actuated periodically, they demonstrated a phase shift and amplitude decay phenomenon proportional to the rate of actuation and inversely proportional to the thermal diffusivity of the SHX. By exploring other widely studied heat transfer problems with periodic boundary condition, I was able to identify the wave number, K, as a key variable in their solutions. Model predictions based on the wave number for a phase shift in cooling fit very well with experimental data, validating the model. Rather than attempting to solve and derive an analytical solution to the fairly complex heat transfer scenario brought about by moving boundaries, I carry out a time scale analysis to gain physical insight. In this process I identify the key time scales for heat transfer (t_k), namely the radial conduction time through the cylinder wall, and compare it to the device time scale (t_d) or the period of actuation. By simple algebraic manipulation I represent the wave number as a dimensionless ratio of the conductive to device time scales. With the use of this dimensionless ratio I quantify to what extent the quasi-static assumption is valid in thermal performance prediction (defined here as < 2% relative error achieved at $t_k/t_d = 10^{-3}$) and when there would be a need for more complex modeling. Furthermore, though equipment limitations prevented experimentally exploring this regime I speculated the effects of entering the regime of $t_k/t_d \gg 1$.

Finally, I discuss the impact of LM micro-droplet shape transition due to tube actuation, which imparts a well-documented anisotropy to the SHX material, on the cooling performance. Through this study, I outline a general approach for designing SHXs undergoing other types of shape deformations in various geometries and highlight otherwise overlooked nuances.

CHAPTER 4

4. CONCLUSIONS AND FUTURE WORK

By conducting systematic theoretical and experimental studies, in this work, I explore the transition from a rigid, static to a soft, stretchable heat exchanger. I split this endeavor into two sequential studies, where, I quantify the effects of surface level deformation in a static framework and I explore a SHX undergoing periodic stretching during operation. The 1st study was done under the context of improving thermoregulatory cooling garments with thermally conductive silicone composites. Here, I developed and experimentally validated a comprehensive thermomechanical model that predicts the total thermal resistance posed by the tubes as a function of its material properties, geometry, substrate properties (skin or metal), and contact pressure.

I found that a major decrease in R'_{tot} to 38 – 50% (all specified resistances correspond to a range set by high and low contact pressure, respectively, relative to a low contact pressure PVC control) is possible by simply changing the tube geometry from circular to rectangular, with optimal width of 5.5 mm for tube wall thickness of 1 mm. The results show that a further substantial decrease of R'_{tot} to 26 – 30 % was achieved by the addition of up to ϕ = 0.3 of the conductive filler. Based on our model, I concluded that the majority of this additional total resistance drop was due to the decrease in the resistance of the tube. In contrast to the substantial reduction in R'_{tube}, increase of ϕ only mildly reduced R'_{int} by 0.1 to 0.2 m°CW^{-1} since potential reduction by a higher composite conductivity was negated by the material stiffening. If this stiffening of the composite

was avoided by using a microscopic liquid metal filler, I estimated that R'_{int} would decrease by another 0.2 to 0.3 m°CW^{-1}, resulting in a R'_{tot} decrease to 20 – 27 %. Alternatively, I propose a potentially safer and cheaper way to achieve a comparable decrease in R'_{tot} via the introduction of an interfacial gel or a thin layer of liquid between the device and the substrate. With insertion of a thin gel layer, I experimentally achieved a R'_{tot} reduction to 22%. Not only was this resistance value very small, it was also pressure-independent in the 0.7 to 6 kPa range, which implies that the contact resistance could not be reduces much further below 0.3 m°CW^{-1}. If the substrate is switched from metal to skin, the model revealed that, due to skin being the softer material, contact resistance is largely independent of the composites' shear modulus. As a result, increasing the contact pressure and ϕ provided a moderately large relative decrease. In contrast to a metal substrate, preventing the stiffening of the composite with use of liquid metal filler would have negligible impact on the contact resistance. Thus, further substantial decrease in R'_{tot} is more effectively achieved by decreasing R'_{int} with insertion of an interfacial layer, which could consist of a simple hydrogel that captures sweat. In turn, sweat and other physiological phenomena such as hair and vaso-constriction/dilation pose the immediate continuation of this work. The thermomechanical model proposed in this work was validated entirely on a metal substrate and though we extrapolated to what we would expect to see on skin, it remains to be validated. These physiological effects can significantly alter how these cooling devices behave, and so capturing the effect on thermal performance of these phenomena unique to skin into a closed form model remains a challenge, both theoretically and

experimentally. However, this work poses a starting point from where a more complex model capturing the unique effects of each physiological effect can be explored.

Next, I demonstrated that by reducing R'_{tot} I can dramatically increase the cooling capability of the devices, allowing for major reduction in the length of tubing required as well as the pump and battery. In our brief treatment of the topic, I illustrated that to achieve optimal performance for a given application, a holistic design approach is required that takes into account not only the total thermal resistance of the tube but also flow regime, temperature distribution along the tube with its resulting device length (size and weight) and pumping power (additional weight). Besides having higher cooling capability and a reduced size, tubes made out of soft, thermally conductive composites that easily stretch beyond 30% could be significantly more ergonomic than current devices. I also point out that besides evaporative heat rejection into vacuum in space applications,[19] current collected-heat rejection methods are short-lasting or excessively heavy (e.g. ice-packs), and in most high-heat load applications LCJs are connected through long "umbilical cords" to heavy, stationary heat sinks (e.g. large ice-chest on-board a vehicle). Consequently, to achieve true portability and long-term applicability in our hot future,[86] efforts along the lines described in this work that focus on design of components that gather heat from the source (i.e. human, robot, electronics) needs to be integrated with development of more compact, lightweight, and energy-efficient methods for rejection of the collected heat into the environment.[31,87] Lastly I note that in some applications significant and sufficiently rapid change in geometry during operation (e.g. stretching of a robotic leg) could produce conditions for which the steady-state

assumption underlying our analysis is invalid, requiring development of a new theoretical framework for device design in such situations.

To begin building a theoretical framework for a transient deformation case, I used liquid metal and silicone composites to develop a single-stream soft heat exchanger and analyzed its thermal performance as it underwent periodic stretching and retraction at varying frequencies during its operation. My experiments revealed that tube actuation causes a decrease of the peak amplitude and causes a phase-shift (φ) in the average spring temperature (ΔT_s), as compared to values collected from stretched but stationary tubes. This phase-lag can be extensive, even causing full inversion of the ΔT_s from that representative of the quasi-static behavior. When analyzed in terms of the ratio of conduction to device actuation time scales (t_k/t_d), all our φ data collapsed into a single general curve. By recasting the wave number in terms of timescales in the classical analytical solution to heat transfer in semi-infinite medium with thermally oscillating boundary condition, I showed that this general curve follows exactly the derived $\varphi = (\pi t_k/t_d)^{1/2}$ relationship. This analysis and my experiments show that soft heat exchanger performance can be predicted with under a 2% temporal deviation (φ) using the quasi-static shape assumption for a t_k/t_d ratio lower than about 10^{-3} (can be thought of as quantification of the $t_k/t_d \ll 1$ condition). As such, I termed these conditions the gradual shape modulation regime. In contrast, when the t_k/t_d ratio increases above 10^{-3} the device performance analysis based on quasi-static shape assumptions would provide an increasingly poor prediction of the system, thus I termed these conditions the rapid shape modulation regime. In this regime, the transient shape effects must be taken into

account for accurate system modeling. While my equipment limitations did not allow me to experimentally probe the regime of $t_k/t_d \gg 1$, my data suggests that eventually the magnitude of oscillation might saturate and, for more thermally conductive tubes, even flatten out. However, in this very rapid shape modulation regime other phenomena are likely to have a significant impact on the soft heat exchanger performance, which presents an interesting area for future exploration. Furthermore, continuation of this work can explore the interaction with additional time scales, such as in the case of a soft, shape changing condenser, and the thermal behavior with various other actuation functions like sinusoidal and sawtooth shape modulation. The combination of the two presents a novel optimization of condensation and shedding via actuation. Although developed here for an elementary soft heat exchanger, our timescale analysis should provide a general framework for the analysis of future soft thermal systems that undergo shape change during operation.

Some applications for SHX devices are already starting to emerge in diverse areas that include personal cooling garments,[33,88] soft robotics for medical applications,[89] cooling for high powered robotics,[46,90] corrosion resistant applications,[62] HVAC,[61] flexible stretchable heating,[86,91,92] and fog harvesting.[93] Adoption of such soft materials would also open-up interesting opportunities for innovative system-level design of compliant, potentially self-adhering, highly-stretchable devices that could include constructal thermofluidic design[94] with combination of liquid-cooled and pure conductive elements in a kirigami-inspired architecture.[95,96] Furthermore, the ease of multimaterial manufacturing stemming from innovations in 3D printing[97] combined with future

enhancements in thermo-mechanical aspects of soft materials will enable many novel soft thermal systems to emerge and potentially outperform their rigid analogues. Design of individual components in such systems could implement the theoretical framework developed in this work, but naturally would require systematic validation in the specific application. However, I hope that this work will facilitate their development by providing a starting point for their thermal design.

REFERENCES

1 M. D. Bartlett and C. Majidi, *Proc. Natl. Acad. Sci.*, 2017, 8–15.

2 R. K. Shah and D. P. Sekulic, *Fundamentals of heat exchanger design*, John Wiley & Sons, 1st edn., 2003.

3 E. H. Wissler, *Human Temperature Control: A quantitative Approach*, Springer, Berlin, Germany, 1st edn., 2018.

4 A. Fassler and C. Majidi, *Adv. Mater.*, 2015, **27**, 1928–1932.

5 R. Tutika, S. H. Zhou, R. E. Napolitano and M. D. Bartlett, *Adv. Funct. Mater.*, 2018, **1804336**, 1–13.

6 E. J. Markvicka, M. D. Bartlett, X. Huang and C. Majidi, *Nat. Mater.*, 2018, **17**, 618.

7 J. Tang, X. Zhao, J. Li, R. Guo, Y. Zhou and J. Liu, *ACS Appl. Mater. Interfaces*.

8 W. Kong, Z. Wang, M. Wang, K. C. Manning, A. Uppal, M. D. Green, R. Y. Wang and K. Rykaczewski, *Adv. Mater.*, 2019, **31**, 1904309.

9 M. I. Ralphs, N. Kemme, P. B. Vartak, E. Joseph, S. Tipnis, S. Turnage, K. N. Solanki, R. Y. Wang and K. Rykaczewski, *ACS Appl. Mater. Interfaces*, 2018, **10**, 2083–2092.

10 M. Ralphs, W. Kong, R. Y. Wang and K. Rykaczewski, *Adv. Mater. Interfaces*, 2019, **1801857**, 6.

11 A. Uppal, M. Ralphs, W. Kong, M. Hart, K. Rykaczewski and R. Y. Wang, *ACS Appl. Mater. Interfaces*, 2020, **12**, 2625–2633.

12 S. A. Nunneley, *Space Life Sci.*, 1970, **2**, 335–360.

13 D. P. Cadogan, *Am. Sci.*, 2015, **103**, 338.

14 B. Conger and J. Makinen, 46th International Conference on Environmental Systems, Houston, 2019, pp. 1–13.

15 Liquid Cooled Garments, *LIQUID COOLED GARMENTS*, Kansas City, 1975.

16 M. M. Yazdi, M. Sheikhzadeh, M. Mokhtari Yazdi and M. Sheikhzadeh, *J. Text. Inst.*, 2014, **105**, 1231–1250.

17 Polar Products. A leading US manufacturer of body cooling and hot & cold

therapy products since 1984, www.polarproducts.com (accessed: February 2019).

18 Veskimo Personal Cooling Systems. www.veskimo.com (accessed: February 2019).

19 Welkins LLC. Welkins provides innovative products and engineering services for applications across medical, military, industrial, and athletic markets, www.welkinsmed.com (accessed: February 2019).

20 J. P. Dionne, K. Semeniuk, A. Makris, W. Teal and B. Laprise, *Thermal manikin evaluation of liquid cooling garments intended for use in hazardous waste management*, Med-Eng Systems Inc., Ottawa, Ontario (CA); US Army Soldier and Biological Chemical Command, Natick, MA (US), 2003.

21 Paxman. Pioneers in Scalp Cooling, www.paxmanscalpcooling.com (accessed: February 2019).

22 Y. Yang, J. Stapleton, B. T. Diagne, G. P. Kenny and C. Q. Lan, *Appl. Therm. Eng.*, 2012, **47**, 18–24.

23 Y. Yang, D. Rana, C. Q. Lan and T. Matsuura, *ACS Appl. Mater. Interfaces*, 2016, **8**, 155778–15787.

24 B. A. Norton, A. M. Coutts, S. J. Livesley, R. J. Harris, A. M. Hunter and N. S. G. Williams, *Landsc. Urban Plan.*, 2015, **134**, 127–138.

25 F. Fornasiero, *Curr. Opin. Chem. Eng.*, 2017, **16**, 1–8.

26 M. Zhao, C. Gao, F. Wang, K. Kuklane, I. Holmér and J. Li, *Int. J. Ind. Ergon.*, 2013, **43**, 232–237.

27 J. K. Tong, X. Huang, S. V Boriskina, J. Loomis, Y. Xu and G. Chen, *ACS Photonics*, 2015, **2**, 769–778.

28 M. Rothmaier, M. Weder, A. Meyer-Heim and J. Kesselring, *Med. Biol. Eng. Comput.*, 2008, **46**, 825–832.

29 Y. Sun and W. J. Jasper, *Build. Environ.*, 2015, **93**, 50–62.

30 G. Zhang, X. Zhang, H. Huang, J. Wang, Q. Li, L. Chen and Q. Wang, *Adv. Mater.*, 2016, **28**, 4811–4816.

31 T. C. Ernst and S. Garimella, *Appl. Therm. Eng.*, 2013, **60**, 316–324.

32 T. Gao, Z. Yang, C. Chen, Y. Li, K. Fu, J. Dai, E. M. Hitz, H. Xie, B. Liu, J. Song, B. Yang and L. Hu, *ACS Nano*, 2017, **11**, 11513–11520.

33 A. D. Flouris and S. S. Cheung, *Ann. Biomed. Eng.*, 2006, **34**, 359–372.

34 P. Webb and J. A. Annis, *Bio-thermal Response to Varied Work Programs in Men Kept Thermally Neutral by Water Cooled Clothing*, Yellow Springs, Ohio, 1967.

35 B. S. Cadarette, S. N. Cheuvront, M. a Kolka, L. a Stephenson, S. J. Montain and M. N. Sawka, *Ergonomics*, 2006, **49**, 209–219.

36 H. Wang, B. Wang, K. Jackson, C. M. Miller, L. Hasadsri, D. Llano, R. Rubin, J. Zimmerman, C. Johnson and B. Sutton, *Transl. Neurosci.*

37 W. Qiu, H. Shen, Y. Zhang, W. Wang, W. Liu, Q. Jiang, M. Luo and M. Manou, *J. Clin. Neurosci.*, 2006, **13**, 995–1000.

38 M. Ridderheim, M. Bjurberg and A. Gustavsson, *Support. care cancer*, 2003, **11**, 371–377.

39 J.-H. Kim, A. Coca, W. J. Williams and R. J. Roberge, *J. Occup. Environ. Hyg.*, 2011, **8**, 409–416.

40 S. L. Davis, T. E. Wilson, A. T. White and E. M. Frohman, *J. Appl. Physiol.*, 2010, **109**, 1531–1537.

41 T. C. Guthrie and D. A. Nelson, *J Neurol Sci*, 1995, **129**, 1–8.

42 R. S. Kovats and S. Hajat, *Annu. Rev. Public Heal.*, 2008, **29**, 41–55.

43 H. J. Thompson, N. C. Tkacs, K. E. Saatman, R. Raghupathi and T. K. McIntosh, *Neurobiol. Dis.*, 2003, **12**, 163–173.

44 N. J. Johnston, A. T. King, R. Protheroe and C. Childs, *Resuscitation*, 2006, **70**, 254–262.

45 F. Wang and W. Song, *J. Therm. Biol.*, 2017, **70**, 37–44.

46 D. Kim, O. Campbell, J. Ahn, L. Sentis and N. Paine, in *Humanoid Robotics (Humanoids), 2017 IEEE-RAS 17th International Conference on*, IEEE, 2017, pp. 710–717.

47 J. T. Kendrick, *Mechanical Engineering Master's Thesis*, Virginia Polytechnic Institute and State University, February 2018.

48 L. Sentis, N. Paine, US Patent Office, Application US20170341227A1, 2017.

49 Y. Yin, Y. Cui, Y. Li, Y. Xing and M. Li, *Appl. Therm. Eng.*

50 R. C. Webb, A. P. Bonifas, A. Behnaz, Y. Zhang, K. J. Yu, H. Cheng, M. Shi, Z.

Bian, Z. Liu and Y.-S. Kim, *Nat. Mater.*, 2013, **12**, 938.

51 Y. Li, X. Shi, J. Song, C. Lü, T. Kim, J. G. McCall, M. R. Bruchas, J. A. Rogers and Y. Huang, *Proc. R. Soc. A*, 2013, **469**, 20130142.

52 Y. Li, Y. Gao and J. Song, *Theor. Appl. Mech. Lett.*, 2016, **6**, 32–37.

53 D. Hill, C. S. Holloway, D. Z. M. Ramirez, P. Smitham and Y. Pappas, *Int. J. Technol. Assess. Health Care*, 2017, **33**, 160–167.

54 L. Greenemeier, *Sci. Am.*, 2008, **298**, 21–22.

55 L. H. Kuznetz, *J. Biomech. Eng.*, 1980, **102**, 155–161.

56 A. B. Chambers and J. R. Blackaby, *A liquid cooled garment temperature controller based on sweat rate*, Moffett Field, 1972.

57 H. Cao, D. H. Branson, S. Peksoz, J. Nam and C. A. Farr, *Text. Res. J.*, 2006, **76**, 587–595.

58 C. W. Katrycz and B. D. Hatton, in *Bioinspired Engineering of Thermal Materials*, Wiley-VCH Verlag GmbH & Co. KGaA Weinheim, Germany, 2018, pp. 129–158.

59 Dignicap. Clinically proven to reduce hair loss from chemotherapyin patients with solid tumors, www.dignicap.com (accessed: February 2019).

60 X. Chen, Y. Su, D. Reay and S. Riffat, *Renew. Sustain. Energy Rev.*, 2016, 60, 1367–1386.

61 C. T'Joen, Y. Park, Q. Wang, A. Sommers, X. Han and A. Jacobi, *Int. J. Refrig.*, 2009, 32, 763–779.

62 J. G. Cevallos, A. E. Bergles, A. Bar-Cohen, P. Rodgers and S. K. Gupta, *Heat Transf. Eng.*, 2012, **33**, 1075–1093.

63 R. W. Style, R. Boltyanskiy, B. Allen, K. E. Jensen, H. P. Foote, J. S. Wettlaufer and E. R. Dufresne, *Nat. Phys.*, 2015, **11**, 82–87.

64 S. H. Jeong, S. Chen, J. Huo, E. K. Gamstedt, J. Liu, S. L. Zhang, Z. Bin Zhang, K. Hjort and Z. Wu, *Sci. Rep.*, 2015, **5**, 1–10.

65 A. Bejan and A. D. Kraus, *Heat transfer handbook*, *Volume 1*, John Wiley & Sons, Inc., Hoboken, New Jersey, 2003.

66 M. G. Cooper, B. B. Mikic and M. M. Yovanovich, *Int. J. Heat Mass Transf.*, 1969, **12**, 279–300.

67 R. S. Prasher and J. C. Matayabas, *IEEE Trans. Components Packag. Technol.*, 2004, **27**, 702–709.

68 R. S. Prasher and C.-P. Chiu, in *Materials for Advanced Packaging*, Springer, New York, 2017, pp. 511–535.

69 K. Rykaczewski, *Temperature*. 2018, https://doi.org/10.1080/23328940.2018.1551706.

70 H. Cao, D. H. Branson, J. Nam, S. Peksoz and C. A. Farr, *J. ASTM Int.*, 2005, **2**, 1–10.

71 T. L. Bergman, A. S. Lavine, F. P. Incropera and D. P. Dewitt, *Fundamentals of heat and mass transfer*, John Wiley & Sons, Inc, New York, 2011.

72 H. Chen, V. V Ginzburg, J. Yang, Y. Yang, W. Liu, Y. Huang, L. Du and B. Chen, *Prog. Polym. Sci.*, 2016, **59**, 41–85.

73 B. Budiansky, *J. Mech. Phys. Solids*, 1965, **13**, 223–227.

74 R. M. Christensen, *Mechanics of composite materials*, John Wiley & Sons, Inc, New York, 2012.

75 S.-Y. Fu, X.-Q. Feng, B. Lauke and Y.-W. Mai, *Compos. Part B Eng.*, 2008, **39**, 933–961.

76 E. H. Kerner, *Proc. Phys. Soc. Sect. B*, 1956, **69**, 808.

77 B. Holt, A. Tripathi and J. Morgan, *J. Biomech.*, 2008, **41**, 2689–2695.

78 M. D. Bartlett, N. Kazem, M. J. Powell-Palm, X. Huang, W. Sun, J. A. Malen and C. Majidi, *Proc. Natl. Acad. Sci.*, 2017, **114**, 2143–2148.

79 M. Denton, *Textiles*. 1972, 3, 12.

80 V. Kumaran, *Sadhana - Acad. Proc. Eng. Sci.*, 2015, **40**, 911–923.

81 M. K. S. Verma and V. Kumaran, *J. Fluid Mech.*, 2012, **705**, 322–347.

82 M. K. S. Verma and V. Kumaran, *Phys. Rev. E - Stat. Nonlinear, Soft Matter Phys.*, 2015, **91**, 1–15.

83 All About Circuits, https://www.allaboutcircuits.com/textbook/direct-current/chpt-12/temperature-coefficient-resistance/.

84 A. Bejan, *Convection Heat Transfer*, John Wiley & Sons, Inc., Hoboken, NJ, USA, 2013.

85 H. S. Carslaw and J. C. Jaeger, *Heat conduction in solids*, Oxford Univ. Press, Cambridge, 1st edn., 1959.

86 K. Rykaczewski, *Temperature*, 2019, **6**, 97–100.

87 D. P. Rini, L. Chow, H. R. Anderson, J. S. Kapat, B. Carman, B. Gulliver, J. M. Recio, *USA US12495279*, 2006.

88 P. Kotagama, A. Phadnis, K. C. Manning and K. Rykaczewski, *Adv. Mater. Technol.*, 2019, **4**, 1800690 (1–12).

89 J. P. D. Shing Shin Cheng,*, Yeongjin Kim, *IEEE Trans Robot.*, 2018, **33**, 986–993.

90 D. Kim, J. Ahn, O. Campbell, N. Paine and L. Sentis, *IEEE/ASME Trans. Mechatronics*, 2018, 1–11.

91 N. S. Jang, K. H. Kim, S. H. Ha, S. H. Jung, H. M. Lee and J. M. Kim, *ACS Appl. Mater. Interfaces*, 2017, **9**, 19612–19621.

92 J. Jang, B. G. Hyun, S. Ji, E. Cho, B. W. An, W. H. Cheong and J.-U. Park, *NPG Asia Mater.*, 2017, **9**, e432–e432.

93 Q. Zhang, G. Lin and J. Yin, *Soft Matter*, 2018, **14**, 8276–8283.

94 A. Bejan and S. Lorente, *Design with constructal theory*, John Wiley & Sons, Inc, Hoboken, 2008.

95 D.-G. Hwang, K. Trent and M. D. Bartlett, *ACS Appl. Mater. Interfaces*, 2018, **10**, 6747–6754.

96 R. Zhao, S. Lin, H. Yuk and X. Zhao, *Soft Matter*, 2018, **14**, 2515–2525.

97 M. A. Skylar-Scott, J. Mueller, C. W. Visser and J. A. Lewis, *Nature*, 2019, **575**, 330–335.

98 B. Saggin, M. Tarabini and G. Lanfranchi, *IEEE Trans. Instrum. Meas.*, 2012, **61**, 489–495.

99 S. Cantournet, R. Desmorat and J. Besson, *Int. J. Solids Struct.*, 2009, 46, 2255–2264.

100 C. H. W. and S. W. G., *Experimental Uncertainty Analysis for Engineers*, 1989.

APPENDIX A

SUPPORTING INFROMATION FOR CHAPTER 2

1. Basic thermal resistance calculation for cylindrical tubes

If we model the LCJ as a single stream heat exchanger with a constant exterior temperature ($T_{ext} = 35$ °C equal to typical skin temperature[70]), the total heat removed from the substrate, $\dot{Q}$, can be predicted using:[71]

$$\dot{Q} = \dot{m}c_p\left(T_{m,out} - T_{m,in}\right) = \dot{m}c_p\left(T_{ext} - T_{m,in}\right)\left(1 - e^{-\frac{1}{\dot{m}c_p R_{tot}}}\right) \qquad \text{(A1)}$$

Where $T_{m,in}$ and $T_{m,out}$ are the mean inlet and outlet temperatures of the liquid, $\dot{m}$ is the internal liquid mass flow, c_p is the specific heat of the cooling liquid, and R_{tot} is the total thermal resistance posed by the wall ($R_{tube} = ln\,(r_o/r_i)/k_w\pi L$), internal convection ($R_{conv} = 1/h_i r_i \pi L$), and skin-tube contact ($R_{int} = R_c/r_o\pi L$). I rather crudely account for the fact that, at most, about half of tube's external circumference is in contact with the warm skin or metallic surface by simply reducing the effective heat transfer area by half in the resistance calculations. Implicitly, I also assume that the outward facing part of the tube is thermally insulated. For a PVC tube with external and internal radii of $r_o = 2$ mm and $r_i = 1$ mm that is typical of LCJs,[33] $R'_{tube} \approx 1$ m°CW^{-1} for one meter of tubing. In turn, the R'_{int} for meter length of tubing (i.e. $L = 1$ m) varies between 0.3 m°CW^{-1} and 1.6 m°CW^{-1} for R_c (contact resistance) in the typical range of 0.002 to 0.01 m^2°CW^{-1}.[98] We highlight that even with a moderate k_w increase to 1 Wm^{-1}°C^{-1} results in of $R'_{tube} \approx$ 0.2 m°CW^{-1}.

In order to calculate R'_{conv}, we need to first estimate h, which is the flow-regime dependent internal convection heat transfer coefficient. To determine the flow regime, I need to calculate the Reynolds number, $Re = D_i V/\nu$ (where $D_i = 2r_i$). With the

kinematic viscosity of water of $\nu \approx 10^{-6}$ m^2s^{-1} at 20 °C and average flow velocity of $V = 4\dot{m}/\rho\pi D_i^2 \approx 0.8$ ms^{-1} for $\dot{m}$ = 2.5 gs^{-1}, $Re \approx 1600$, which indicates that the flow is laminar. Neglecting entry length effects, the following correlation can be used to calculate the Nusselt number, Nu_D, for constant exterior boundary condition:[71]

$$Nu_D = \frac{hD_i}{k} = 3.66 \quad \text{(A2)}$$

With k_w being the thermal conductivity of water equal to about 0.6 $Wm^{-1}°C^{-1}$ at 20 °C, $h = k_w Nu_D/D_i \approx 1100$ $Wm^{-2}°C^{-1}$. Correspondingly, $R'_{conv} \approx 0.3$ $m°CW^{-1}$ (for half-heated tube), and since there is no dependency to ϕ, convection resistance acts as a flat contribution to the total resistance. If the flow rate was increased so that Re is over around 2300, the flow begins to transition to turbulent (fully turbulent flow is achieved at Re > 10000). To estimate the Nusselt number in this regime, one can use the Dittus-Boelter correlation:[71]

$$Nu_D = 0.23Re^{0.8}Pr^{0.4} \quad \text{(A3)}$$

Where Pr is the Prandtl number. For example, for $\dot{m}$ =16.6 gs^{-1} of water, $h \approx 25000$ $Wm^{-2}°C^{-1}$ and $R'_{conv} \approx 0.01$ $m°CW^{-1}$. Consequently, in laminar regime the convective thermal resistance has a noticeable contribution to the total resistance. In turn, in the turbulent regime the convective thermal resistance is negligible comparing to that posed by the wall and the wall-skin contact. It is also important to mention that, despite the Re based on the average speed in our experiment indicating a laminar flow, it is likely that in my setup the transition to turbulence was tripped because of the use of the peristaltic pump. Specifically, without a flow dampener, the flow pulsates significantly with each "liquid-slug" that is propelled by this positive-displacement pump. To confirm this, I

added tracer particles to the flow and were able to visually confirm signs of turbulent flow. Furthermore, there have been studies[80,82] that demonstrate the transition to turbulence (thus enhancing mixing and heat transfer) at subcritical values of Re number (<2300) for flows in soft tubes. Consequently, I assume that heat transfer coefficient is higher than one predicted from laminar flow correlation, thus R'_{conv} can be safely neglected as compared to R'_{int} and R'_{tube}.

2. Aluminum particle size-distribution

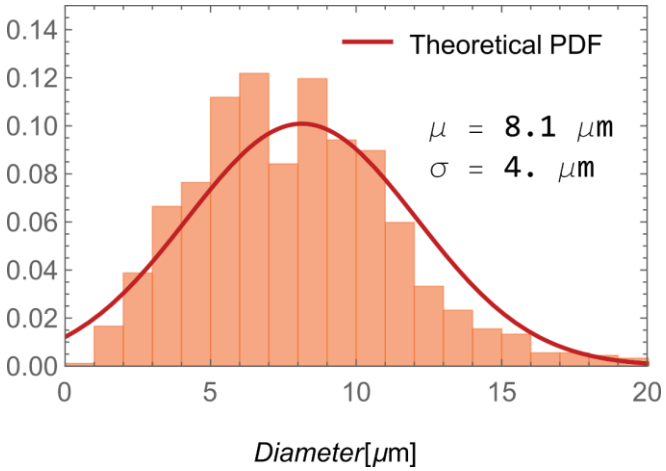

Figure A1: Plot of measured and modeled aluminum particle size distribution.

3. Geometric model of average surface roughness increase with filler content

If we assume that spherical particles with radius r_p are evenly distributed on a regular cubic array with unit cell side size of a, the filler volume fraction is equal to:

$$\phi = \frac{4\pi r_p^3}{3a^3} \tag{A4}$$

By rearranging above equation, we obtain:

$$a(\phi, r_p) = \left(\frac{4\pi}{3\phi}\right)^{1/3} r_p \tag{A5}$$

Assuming the particle array extends to the composite surface, the number of particles per a trace line we would encounter, n_{line}, scales with $1/a$. If we further assume that, on average, the particles extend about half way above the composite surface, we can calculate the contribution of each of the particles to the normalized average surface roughness, $\sigma_{a\ per\ particle}$, as:

$$\sigma_{a\ per\ particle}\ (r_p) = \frac{1}{r_p}\int_0^{r_p}\sqrt{r_p^2 - y^2}\,dy = \frac{\pi}{4}r_p \tag{A6}$$

To calculate the total normalized increase of average surface roughness, I multiply $\sigma_{a\ per\ particle}$ by n_{line} and substitute Equation A5:

$$\sigma_{a\ increase}\ (\phi) = n_{line}\sigma_{a\ per\ particle} = \frac{\pi r_p}{4a} = \frac{\pi r_p}{4\left(\frac{4\pi}{3\phi}\right)^{1/3} r_p} = \frac{\pi}{4\left(\frac{4\pi}{3}\right)^{1/3}}\phi^{1/3} \approx \frac{\phi^{1/3}}{2} \tag{A7}$$

Since surface has some inherent roughness at $\phi = 0$, $\sigma_a\ (0)$, the absolute increase of surface roughness with ϕ can be expressed as:

$$\sigma_a\ (\phi, r_p) = \sigma_a\ (0) + r_p\frac{\phi^{1/3}}{2} \tag{A8}$$

If $\sigma_a\ (0) \approx r_p$ as in our case, I can simplify Equation A8 to:

$$\sigma_a\ (\phi) = \sigma_a\ (0)\left(1 + \frac{\phi^{1/3}}{2}\right) \tag{A9}$$

In turn, for normalized root-mean-square surface roughness increase per particle ($\sigma_{RMS\ per\ particle}$):

$$\sigma_{RMS\ per\ particle}\ (r_p) = \sqrt{\frac{1}{r_p}\int_0^{r_p}\left(\sqrt{r_p^2 - y^2}\right)^2 dy} = \sqrt{\frac{2}{3}}r_p \tag{A10}$$

To calculate the total increase of normalized root-mean-square surface roughness, I multiply $\sigma_{RMS\ per\ particle}$ by n_{line} and substitute Equation A5:

$$\sigma_{RMS\ increase}(\phi) = n_{line}\sigma_{RMS\ per\ particle} = \sqrt{\frac{2}{3}}\frac{r_p}{a} = \sqrt{\frac{2}{3}}\frac{r_p}{\left(\frac{4\pi}{3\phi}\right)^{1/3} r_p} = \frac{\sqrt{\frac{2}{3}}}{\left(\frac{4\pi}{3}\right)^{1/3}}\phi^{1/3} \approx \frac{\phi^{1/3}}{2} \quad \text{(A11)}$$

Since surface has some inherent roughness exists at $\phi = 0$, $\sigma_{RMS}(0)$, the absolute increase of σ_{RMS} with ϕ can be expressed as:

$$\sigma_{RMS}(\phi, r_p) = \sigma_{RMS}(0) + r_p\frac{\phi^{1/3}}{2} \quad \text{(A12)}$$

If $\sigma_{RMS0} \approx r_p$ as in my case, I can simplify Equation A12 to:

$$\sigma_{RMS}(\phi) = \sigma_{RMS}(0)\left(1 + \frac{\phi^{1/3}}{2}\right) \quad \text{(A13)}$$

The plot in Figure A2a and A2b show that with $\sigma_{a0} = 10.0$ μm and $\sigma_{RMS0} = 12.2$ μm values calculated using Equation A9 and Equation A13 match well with my experimental measurements (see example line scans in Figure A3).

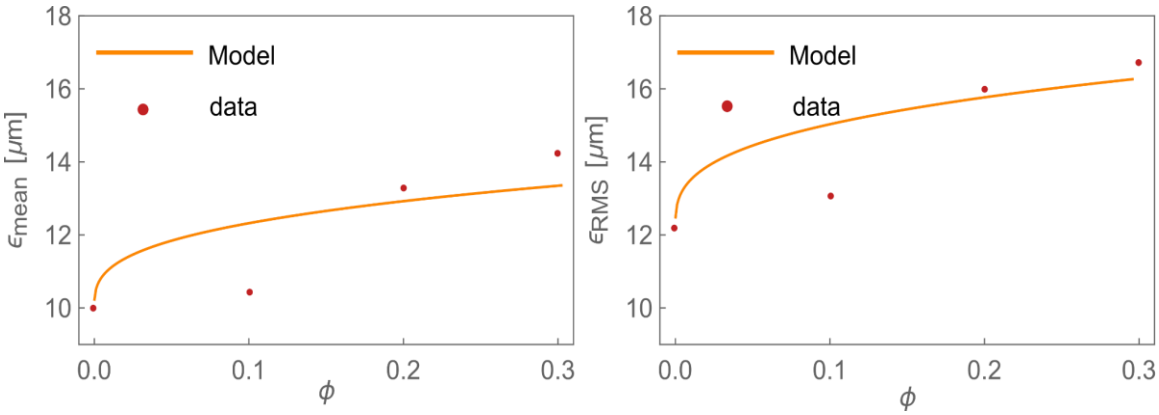

Figure A2: Plot of measured and modeled (a) average and (b) root-mean-square surface roughness of the silicone-aluminum particle composites.

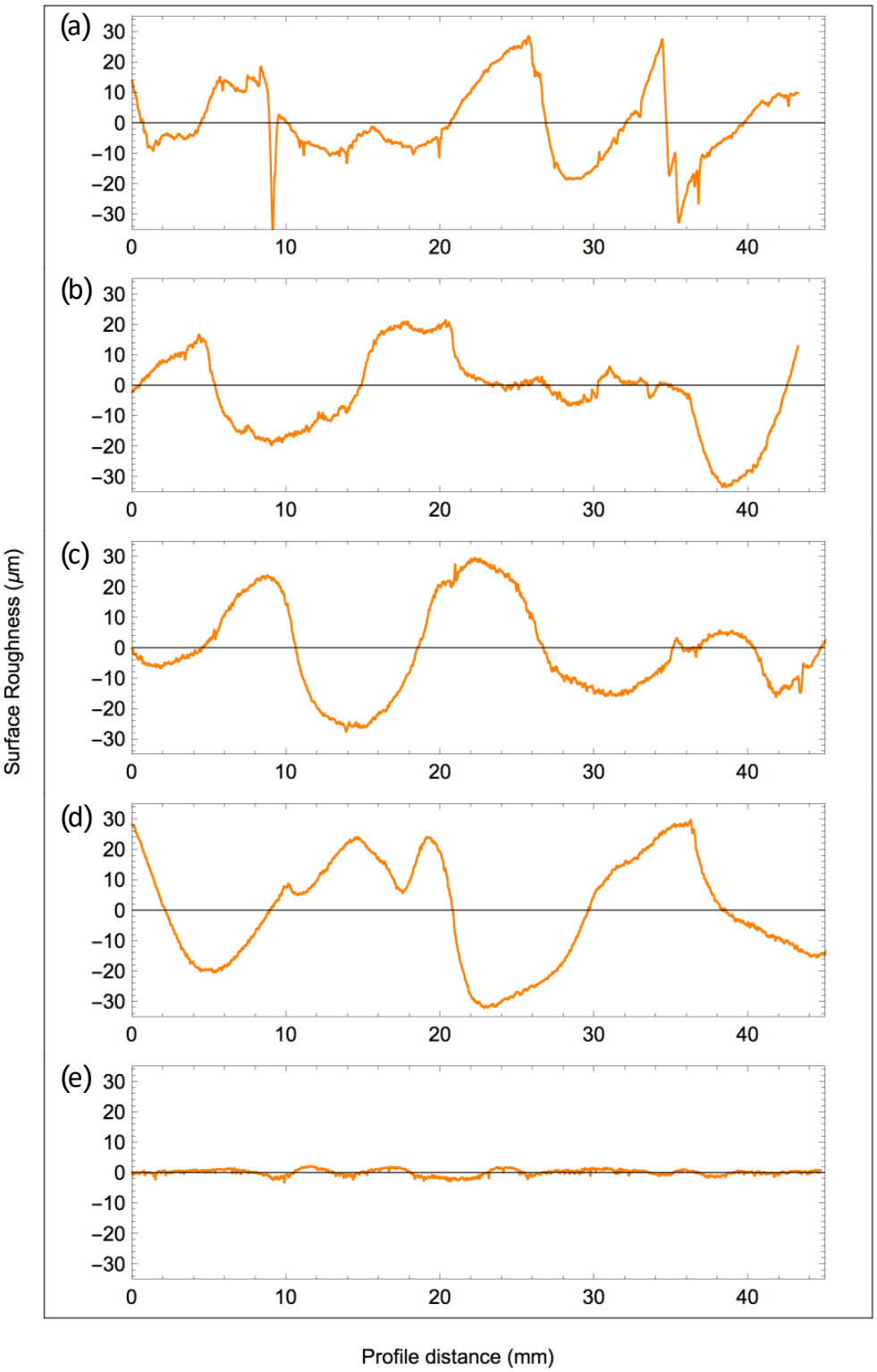

Figure A3: Example surface roughness line scans for composite devices with ϕ of (a) 0, (b) 0.1, (c) 0.2, and (d) 0.3 as well as (e) of the polished metal surface of the heater.

4. Young's and Shear Moduli

In Figure A4 I demonstrate typical stress strain curves and demonstrate each device is capable of being stretched to at least 30 % its original length while being in the elastic region. I further demonstrate there is a decrease in the ultimate stress and strain experienced with increase in filler fraction. Studies have shown[99] that with the addition of filler particles there is an increase strain hysteresis and filler silicone composites tend to present a loss of stiffness under cyclic loading. Thus, in Figure A4a I cycle samples to explore any effects of increasing filler particles. It can be seen that with increasing filler, the hysteresis effect does tend to widen. As such, the effect of filler particles on LCJ durability requires extensive testing which is beyond the scope of this work.

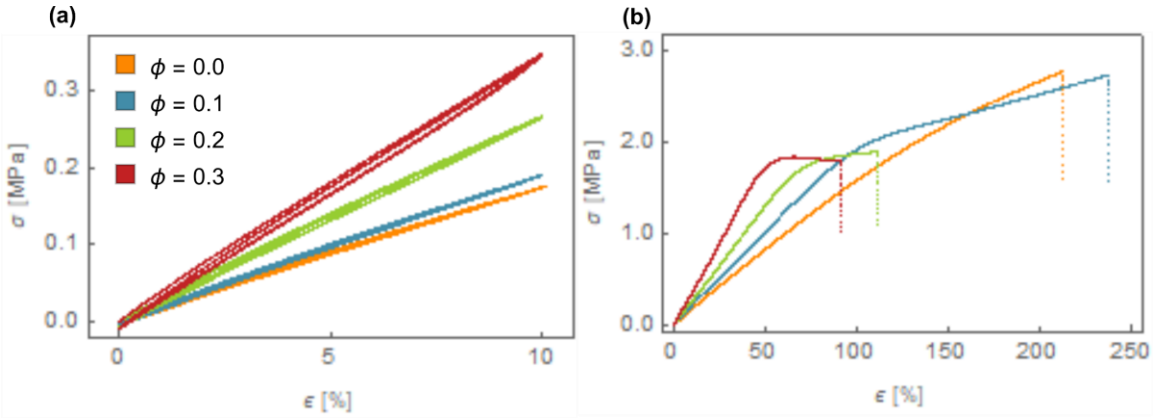

Figure A4: (a) Example stress-strain plots for up to 10% strain from which Young's Modulus was calculated – includes one cycle for each filler, (b) stress-strain plots for samples stressed to break.

With regards to shear modulus, I note that I report values of storage modulus G' from the tests as the shear modulus since the loss modulus of a fully cured sample is negligible (see Figure A5), thus:

$$G = \sqrt{G'^2 + G''^2} \approx G' \tag{A14}$$

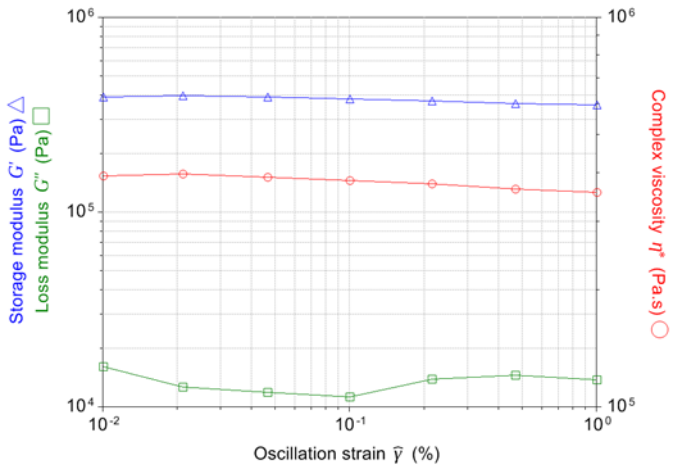

Figure A5: Example of Small Oscillatory Shear Rheology results for the silicone matrix.

Accordingly, I report the average shear modulus for each filler configuration based on four samples along with the 95% confidence interval calculated as below:

$$G_{CI} = G_{mean} \pm \frac{t\,s}{\sqrt{n}} \tag{A15}$$

Where, n is the number of samples, s is the standard deviation and t is the student's t-value corresponding to 95% confidence interval, *i.e.* $\alpha = 0.05$ and $n = 4$.

5. Thermocouple Calibration

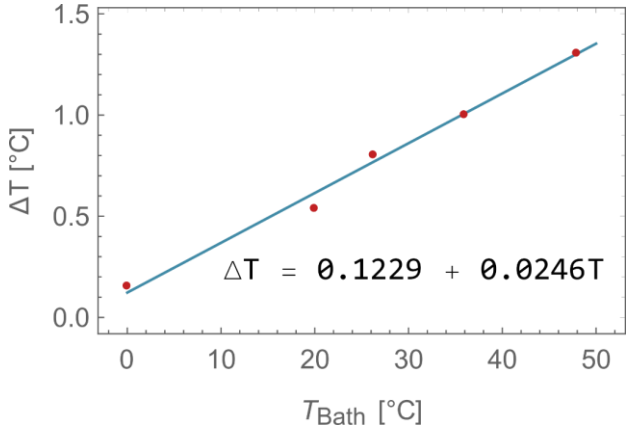

Figure A6: Thermocouple calibration curve

Prior to setup, I calibrated the four T-type thermocouples, which were rated as 'special limits of error' and so +/- 0.3°C, against a Class A Pt 100 RTD, rated as +/-

0.1°C. The calibration process consisted of measuring the temperature of a continuously stirred water bath at four different steady state temperatures using all five sensors. The thermocouples were found to drift at higher temperatures and thus, based on the difference of the thermocouples to the RTD, a calibration curve was used to correct for the drift.

6. Shape-factor calculations and FEM simulations

We compare $R'_{tube}(\phi)$ estimated by FEM simulations of the exact cross-section of our devices performed using Comsol Multiphysics (see the cross-section schematic in Figure A7a) and calculated two shape factors. Specifically, I compare simulations to analytical predictions for a long, horizontal, isothermal cylinder buried in a semi-infinite medium ($S_{semi-infite} = 2\pi L_{tube}/cosh^{-1}(2z/D_i)$, see Figure A7c) and for a horizontal cylinder of length L_{tube} midway between two parallel planes of equal length and infinite width ($S_{finite} = \pi L_{tube}/ln(8z/\pi D_i)$, see Figure A7d). The shape factors for a meter of tubing are obtained by setting $L_{tube} = 1$ m. The corresponding two-dimensional steady-state FEM simulation were conducted with following parameters: z =2 mm, L_{tube} = 1 m, w = 3, 4, and 5.5 mm, $D_i = 2$ mm, $h = 4$ mm, h_{ins} = 0.9 mm, k_m = 0.3 $Wm^{-1}°C^{-1}$, and k_c varied between 0.3 and 2 $Wm^{-1}°C^{-1}$ (see example results in Figure A7b). For all layers, free quad mesh geometry with "Fine" size was utilized. The bottom surface of the device was set to 35 °C and the internal surface of the channel was set to 20 °C, while all other surfaces were assumed to be thermally insulated. The simulation was also repeated with internal convection boundary condition inside the cylinder which, in agreement with my preliminary resistance calculations, showed that R_{conv} provides only a minor effect.

The plot in Figure A7e shows that R'_{tube} calculated using the "finite" shape factor approach is close to simulation values with w = 3 mm and 4 mm and agrees exactly with simulation results for w = 5.5 mm (my device geometry).

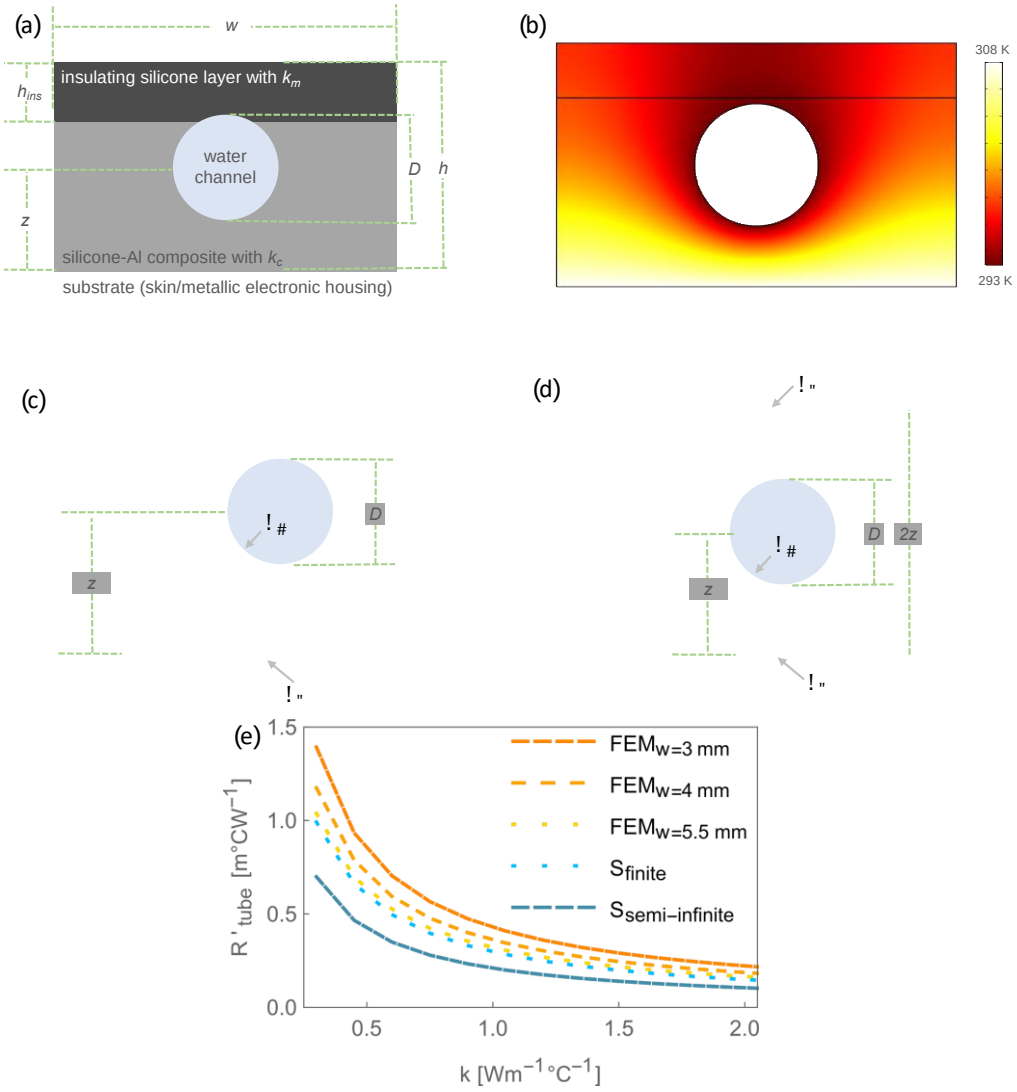

Figure A7: (a) schematic of the device cross-sectional geometry, (b) example temperature distribution obtained using FEM simulation, and schematics of the geometries corresponding to shape factor formulas for (c) cylinder buried in a semi-infinite medium and (d) and for a horizontal cylinder midway between two parallel planes of equal length and infinite width; (e) plot comparing thermal resistance of the tube wall for meter of tubing estimated using the two analytical shape factor models and obtained from FEM simulations as a function of the thermal conductivity of the silicone-aluminum composite layer.

7. Full expanded expressions for $R'_{int}(\phi)$

The final expression for $R'_{int}(\phi)$ for tube-metal substrate contact (i.e. robotic cooling case) is obtained by substituting expressions for Equation A4 for $k_c(\phi)$, Equation 6 for $G_c(\phi)$, and Equation A10 for $\sigma_{c-RMS}(\phi)$:

$$R_{int-1}(\phi) =$$

$$\left(41.9\left(\frac{G_m}{P(1-2.5\phi)}\right)^{\frac{1}{4}}\left(k_m^2(\phi-1)-k_pk_m(\phi+0.5)-k_mk_{sub}(0.5\phi+1)+k_pk_{sub}(0.5\phi-0.5)\right)\right.$$
$$\left.*\left(\sigma_{c-RMS}^2(0)\left(1+0.5\phi^{\frac{1}{3}}\right)^2+\sigma_{sub-RMS}^2\right)^{\frac{1}{2}}\right)/$$

$$\left(k_{sub}k_mL_cw\left(k_m\phi-k_m-0.5k_p-k_p\phi\right)\right) \quad \text{(A16)}$$

In turn, in the case of silicone device-skin interface the appropriate expression for thermal contact resistance is:

$$R_{int-2}(\phi) =$$

$$\left(41.9\left(\frac{G_{skin}}{P}\right)^{\frac{1}{4}}\left(k_m^2(\phi-1)-k_pk_m(\phi+0.5)-k_mk_{sub}(0.5\phi+1)+k_pk_{sub}(0.5\phi-0.5)\right)\right.$$
$$\left.*\left(\sigma_{c-RMS}^2(0)\left(1+0.5\phi^{\frac{1}{3}}\right)^2+\sigma_{sub-RMS}^2\right)^{\frac{1}{2}}\right)/$$

$$\left(k_{sub}k_mL_cw\left(k_m\phi-k_m-0.5k_p-k_p\phi\right)\right) \quad \text{(A17)}$$

8. Pressure loss measurements and discussion

I compare the pressure difference between the inlet and outlet of the channels for devices with varying filler fraction. I find our devices are offset by about 15 kPa as compared to the control PVC device (see Figure A8a) and this is likely caused by the nature of the device fabrication process. Since I use steel rods to define the channels, the roughness of the steel rods is imparted on the inner surfaces of the channels. In turn, my devices have an inner wall roughness of about 50 µm (typical for drawn steel), which results in a pressure drop offset compared to the smooth finished PVC tubes. I find that the addition of filler particles initially, from 0 – 0.1, result in a decrease in pressure drop from 92.7 to 85.4 kPa and for $\phi = 0.1, 0.2$, and 0.3, there is gradual increase in pressure drop. I postulate that this increase in due to an increase in the inner surface roughness of the tubes as function of filler content. Since the particles (8 µm) are in the order of the expected surface roughness of steel rods (50 µm), they are capable of increasing the surface roughness of the inner wall. Naturally, this effect is magnified with increasing filler content. However, in this work I have not extensively studied the effect of filler and modulus on pressure drop and it is recommended for future work.

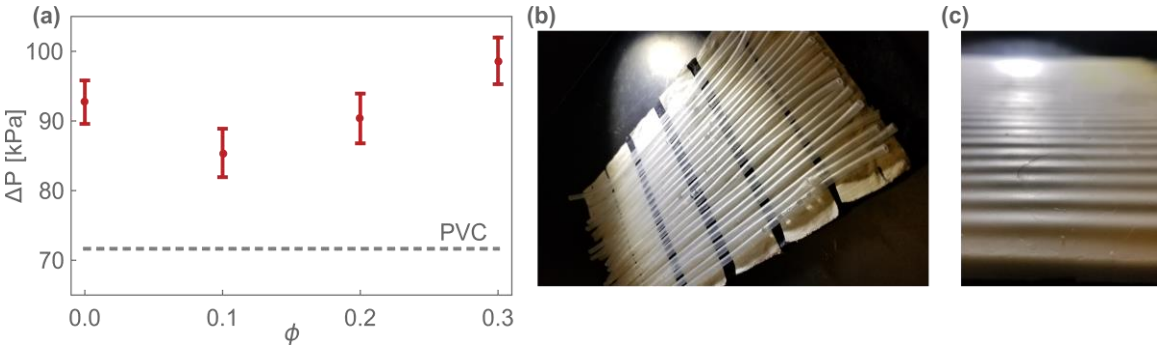

Figure A8: (a) Pressure loss data for each filler fraction device. The flat line indicates the pressure loss for the control PVC device. (b) The control PVC device (c) Observed inflation in softer devices made from Smooth-On 14 NV.

9. Cooling performance of low resistance LCJs

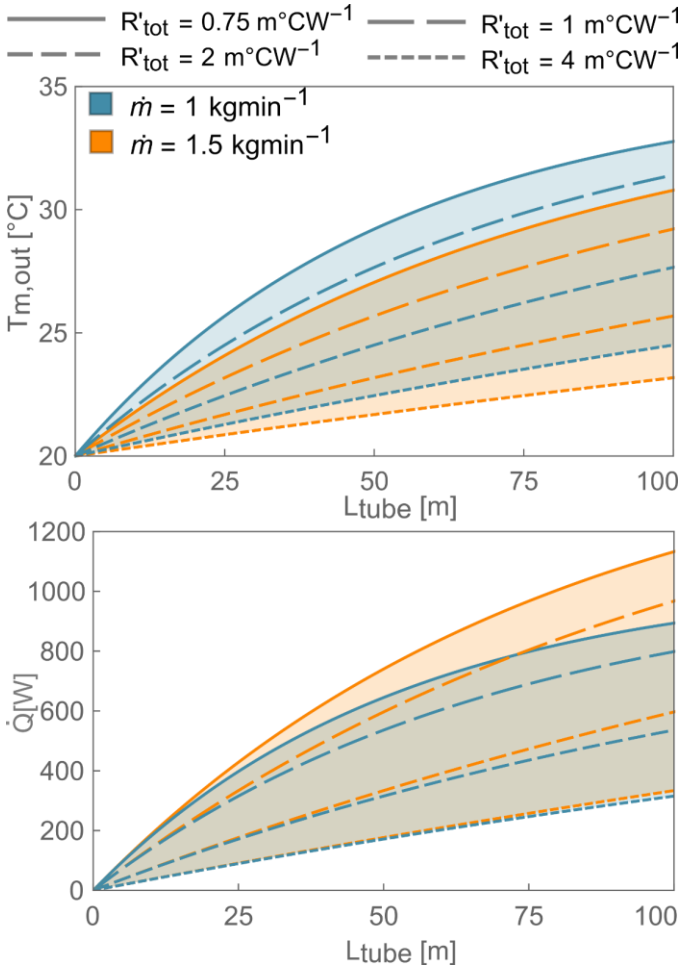

Figure A9: Cooling performance of up 100 m of tubing with various resistances and flow rates.

10. Uncertainty Analysis

In table A1, I list the measured variables and their respective biases that propagate uncertainty in the measurement of R_{tot}.

Variable	Bias (b_x)	Standard Deviation (s_x)
Temperature (T)	+/- 0.28 °C	0.005 °C
Flow Rate ($\dot{V}$)	+/- 3 ml/min	0.5 ml/min
Length (L)	+/- 0 mm	+/- 1 mm

Table A1: List of biases and standard deviations taken into account and applied in the Taylor series method for the propagation of uncertainty.

The Taylor Series Method[100] states the standard uncertainty is given as a combination of systematic and random standard uncertainties expressed as:

$$u_r^2 = \sum_{i=1}^{J} (\frac{\partial r}{\partial X_i})^2 b_{x_i}^2 + \sum_{i=1}^{J} (\frac{\partial r}{\partial X_i})^2 s_{x_i}^2$$

Where, r represents the variable of interest (R'_{tot}) in my case, X_i represents every variable used in the calculation of r, and, b and s represents the bias and standard deviation of each X_i, respectively. Thus, after manipulating the equation for R'_{tot} to be a subject of an equation including all the base variables and taking the partial derivatives, the uncertainties were computed. The error bars in the main text represents a 95% confidence interval, which is 2x of u_r.

APPENDIX B

SUPPORTING INFROMATION FOR CHAPTER 3

1. Liquid metal droplet size-distribution

The liquid metal micro-drop size was measured by image processing a microscope image of a silicone composite (made possible due to the use of a transparent silicone) for over 100 droplets.

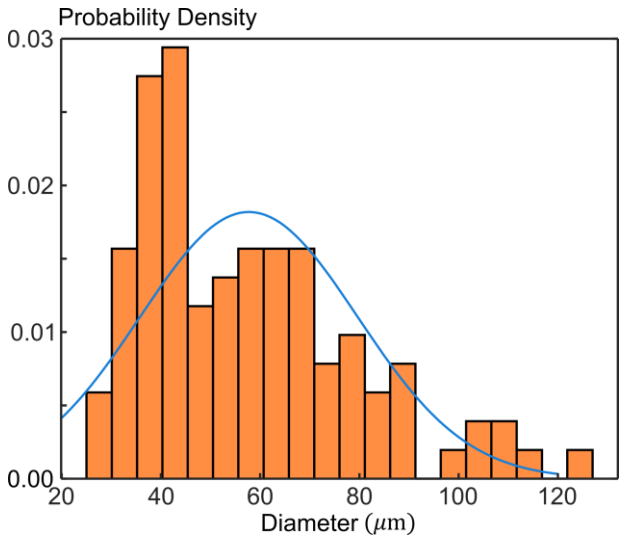

Figure B1: Plot of measured liquid metal particle size distribution

2. Casting Process

To make the stretchable heat exchangers, I cast two forms of silicone rubber stoppers to provide compression-based alignment and plugging. The fishing line was centered with the glass tube using rubber stoppers at both ends with an outer diameter (OD rubber stopper) slightly larger than the inner diameter of the glass tube (>5.6 mm) and inner diameter slight smaller than fishing line (<1.9 mm under tension). To align the spring with the fishing line, I cast silicone pieces (ID rubber stopper) with threading and an inner diameter less than 1.9 mm. The spring was threaded into each of these pieces on both sides and pulled along the fishing line from 160 to 275 mm, pre-extending the spring, and since the inner diameter of the stopper was smaller than the fishing line there

was enough constriction force on the fishing line to keep the end pieces in place and the spring extended. This configuration was hung vertically and the precured silicone was injected from the bottom at a slow rate of 0.5 ml/min to prevent cavity formation. Once filled, the fishing line was pulled through from the bottom and a weight was hung from it to maintain tension and align the setup vertically. This was allowed to cure at lab temperature for 16 hours and the tubes were removed with the help of IPA as a lubricant.

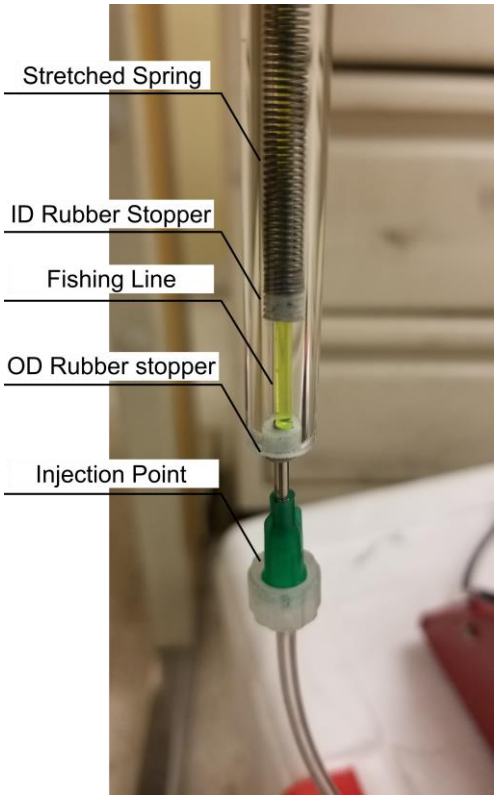

Figure B2: Picture of the tube casting prior to injection of the silicone composite.

3. Linear actuator calibration

The linear actuator was calibrated to convert the resistance read from the inbuilt potentiometer to the length of stretch, measured relative to the beginning of the stretchable section. Additionally, rates of extension and retraction were measured, and the best fit equation was used to set certain rates on the actuator. The slight deviation from linearity and variations between rates of extension and retraction cause the somewhat arbitrary rates seen in this study. However, note that I use actual rates calculated from each run for my device time scale calculations.

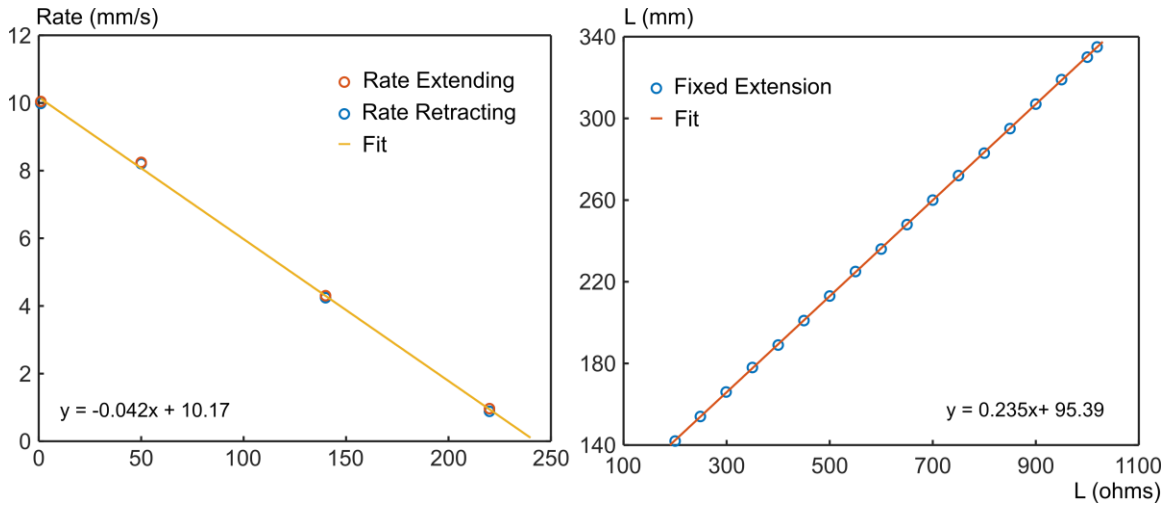

Figure B3: Plots of the calibration carried out on the linear actuator for the rate of actuation and length stretch vs resistance on the actuators inbuilt potentiometer

4. The mechanical behavior of the tubes

The Poison's effect describes the tube behavior as:

$$D = D_0 \left(\frac{L}{L_0}\right)^{-\nu}$$

I compared my experimental measurements of diameter versus simple simulations for fully constrained and unconstrained tubes made of hyper elastic materials (Comsol Multiphysics 5.2). As clearly seen in Figure B4, I see an in-between behavior in the shaded region between the two simulations. Additionally, the contraction due to thermal expansion can be seen by comparing the orange lines (2A of heating current) versus the blue lines (no heating).

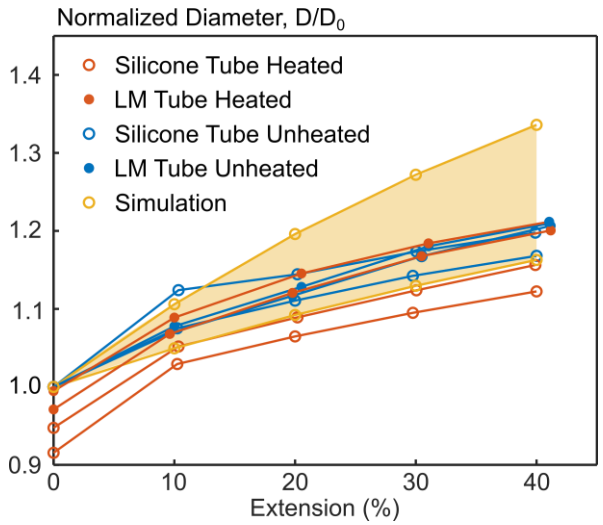

Figure B4: Plot demonstrating the pseudo constrained behavior of the tube mechanics and the effect of thermal expansion constricting the inner diameter due to thermal expansion

5. The temperature coefficient of the tube-embedded extension spring

The tubes cast with embedded springs were submerged in heated, well mixed, water or silicone oil baths. In this configuration, the baths were allowed to cool down or heat up and the spring resistance versus the bath temperature was transiently measured. This was done for four tubes of which the data was demeaned and compiled to one set of data and used to measure the temperature coefficient. A reference resistance was evaluated at temperatures close to 70°C, for each tested tube.

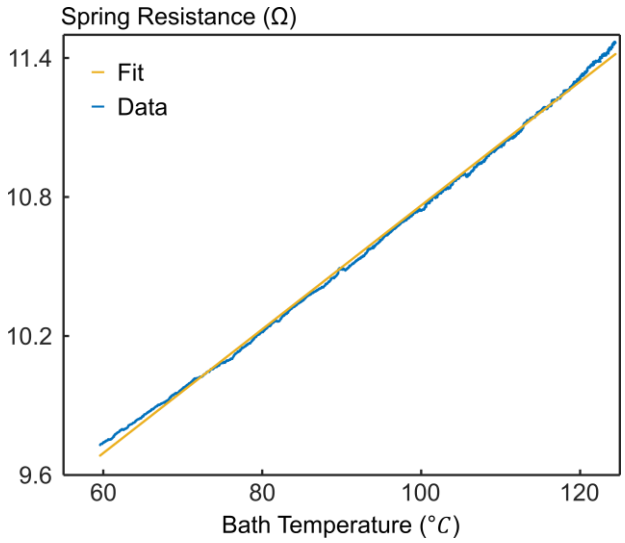

Figure B5: An example curve of the spring electrical resistance vs bath temperature with a linear fit. One of 4 runs used to evaluate temperature coefficient of resistivity of the embedded spring.

6. The effectiveness of the exterior tube insulation during actuation

The electrical resistance of the spring fluctuates with deformation (due to the associate cooling variation) and so there is a slight fluctuation in heat supply, illustrated by the nearly flat line seen in Figure B6 approximately +/- 1 W. In turn, due to a combination of flow fluctuation and tube deformation, the heat gained by the water also fluctuates. However, it oscillates about Q_{supply} indicating an effective insulation.

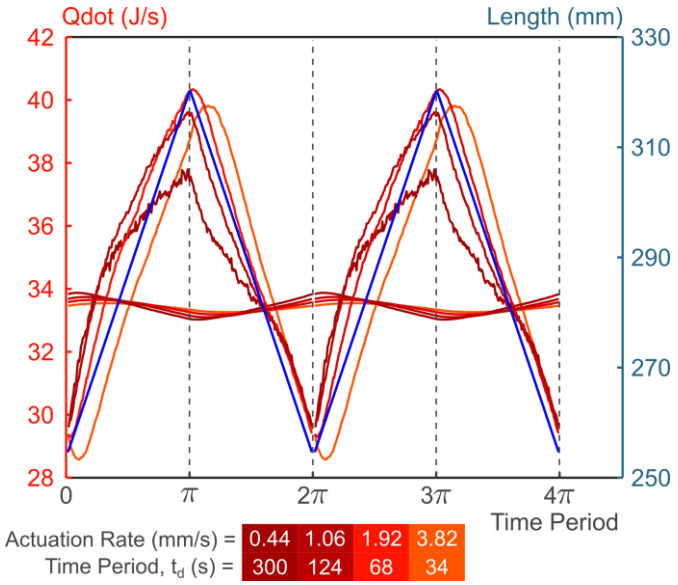

Figure B6: Plot demonstrating oscillations in Q_{in} with actuation about the calculated Q_{supply}, demonstrating the effectiveness of insulation in this system.

7. Uncertainty Analysis

In Table B1, I list the measured variables and their respective biases that propagate uncertainty in the calculation of t_k/t_d.

Variable	Bias (b_x)
Diffusivity (T)	+/- 5 %
Tube Thickness (V̇)	+/- 0.1 mm
Length (L)	+/- 1 mm
Rate of Actuation (L′)	+/- 0.1 mm/s

Table B1: List of biases taken into account and applied in the Taylor series method for the propagation of uncertainty of the time scales.

The Taylor Series Method[100] states that the standard uncertainty is given as a combination of systematic and random standard uncertainties expressed as:

$$u_r^2 = \sum_{i=1}^{J} (\frac{\partial r}{\partial X_i})^2 b_{x_i}^2 + \sum_{i=1}^{J} (\frac{\partial r}{\partial X_i})^2 s_{x_i}^2$$

Where, r represents the variable of interest (t_k/t_d) in our case, X_i represents every variable used in the calculation of r, and, b and s represents the bias and standard deviation of each X_i, respectively. Standard deviations are much lower than the bias in my measurements and so I mainly consider the biases. Thus, after manipulating the equation for t_k/t_d to be a subject of an equation including all the base variables and taking the partial derivatives, the uncertainties were computed. The error bars in the main text represents a 95% confidence interval. The bias of thickness was computed with the same method, where the Taylor series uncertainty was run for the Hagen-Poiseuille law for pressure drop with the biases of each variable listed below.

Variable	Bias (b_x)
Viscosity (μ)	+/- 1.24E-5 $Pa.s$
Pressure Drop (ΔP)	+/- 20 Pa
Length (L)	+/- 1 mm
Flow Rate (V̇)	+/- 3 ml/min

Table B2: List of biases taken into account and applied in the Taylor series method for the propagation of uncertainty of diameter.

APPENDIX C

COPYRIGHT PERMISSIONS

Copyright permissions

Reproduced from Ref. 88 with permission from Advanced Material Technologies Wiley. Rights to reproduce in this work have been requested and acquired.

Reproduced with permission from the Royal Society of Chemistry. Open rights when reproducing in a thesis. Publication in review.